CARMA Memorandum Series #55

CARMA SUMMER SCHOOL 2010

Melvyn Wright, Marc Pound, Dick Plambeck, John Carpenter, Nikolaus Volgenau, Tom Culverhouse, Doug Friedel, Swarnima Manohar, Thiago Goncalves, Mislav Baloković, David Fisher, Rodrigo Herrera Camus, Katie Jameson, Ben Westbrook, Zubair Abdulla, Felippe Navarrete, Rie Miura, Adele Plunkett, Jason Speights, Tim Weinzirl, Manuel Merello, Thomas Fok Kai Tung, Marc Royster, Zubair Abdulla

October 1, 2010

ABSTRACT

The third CARMA Summer School was held at the observatory on Cedar Flat 2010 July 11-17 with 17 students from Berkeley, Caltech, Illinois, Maryland, U. Chicago, U. Texas, Max Planck Institute for Radioastronomy, U. Tokyo, Yale,U. Hong Kong, U. Split, and Northwestern. During the school, students formed small teams and designed and obtained their own observations, in consultation with the instructors. Observations were of evolved stars, protostars, galaxies, molecular clouds, and SZ clusters. In this memo we collect together some of the results from the student projects.

1. Introduction

The fourth CARMA Summer School was held at the observatory on Cedar Flat 2010 July 11-17 with 19 students from Berkeley, Caltech, Illinois, Maryland, U. Chicago, U. Texas, Max Planck Institute for Radioastronomy, U. Tokyo, Yale,U. Hong Kong, U. Split, and Northwestern.

The school had the use of the telescope for the week. The array was in the compact E-configuration. During the school the students had their own observing projects which they worked on during the week as well as attending lectures and demonstations. Each of the student projects had 5-6 hours of telescope time and the students controlled the telescope for their own projects. The students took the observations, reduced the data, analyzed and presented the results.

On Monday the students learned how to select suitable observing projects for the CARMA telescope. The introductory lectures covered the characteristics of the telescope, instrumentation, and observing techniques. The students learned how to:
1) select suitable astronomical sources for observing.
2) select the observing frequency, spectral lines to be observed.
3) evaluate angular resolution, velocity resolution and sensitivity needed.
4) select the correlator setup and calibrations needed.
5) prepare an observing script to define the observing procedure at the telescope.
6) make the observations

During the rest of the week, the lectures and demonstrations covered the theory and techniques used for millimeter wavelength aperture synthesis and the CARMA array. As they worked on their projects the students learned how to:
7) schedule the telescope effectively.
8) calibrate the data.
9) make images.
10) identify and fix problems that set off the alarm.
11) analyze and present the results.

On Friday the students made 10-15 minute presentations and we discussed the results. In all, a very satisfying week seeing all the enthusiasm and so many exciting projects from initial planning and observations, to analysis and results.

2. The CARMA Telescope

The CARMA telescope is designed as an aperture synthesis telescope. There are two receiver bands: 3 mm and 1 mm. A basic aperture synthesis observation makes an image the size of the primary beam ($\lambda/D \sim 1'$ at 100 GHz; $0.5'$ at 230 GHz) with a resolution corresponding to the maximum separations of the 15 antennas. You will learn how this works at the school. During the school, the telescope was in the most compact antenna configuration, the E-configuration, which gives an angular resolution of $\sim 10''$ at 100 GHz, and $\sim 5''$ at 230 GHz.

The most convenient source size is one which is smaller than the size of the primary beam when only one pointing is needed. Larger sources can be imaged by time-sharing the pointing of the antennas (mosaicing), at the cost of lowered sensitivity.

The sensitivity is determined by the system noise (receivers plus atmosphere), the bandwidth (or velocity resolution), and the observing time. The atmosphere is usually not so good for 1 mm observations in the summer, or for sources which are at low declinations and must be observed through more of the atmosphere, so it's best to select a bright source which is high in the sky and can be observed at 3 mm, It's best to observe a strong enough source that we can make an image during the school, rather than a detection project, then we can see the effects of different imaging techniques.

Some of the projects that the students wanted to do did not satisfy all these conditions. We put the data on disk where it could be reduced by multiple students, so we could compare the results using different data reduction methods, and the students could work on different types of projects (single pointing, mosaics, continuum, spectral line etc.)

On the Cedar Flat website, technical description of the array is available as are tools to calculate sensitivity, visualize the correlator setup, and locate bright calibration sources.

2.1. Logistics

Because this is a 'hands-on' school, all lectures and demonstrations were held in the control building and at the telescopes at Cedar Flat. Mel, Marc, Dick and 9 of the students stayed in the 'Nelson' group campground, about 1.5 miles from the control room, and near the antenna pads for the A-configuration. Those who camped avoided the hassle of driving up and down the mountain each day and had a wonderful opportunity to star-gaze each night. The other students stayed in the dorm and cottage at OVRO. Delicious breakfasts, lunches, and dinners were provided at the observatory, prepared by Terry Sepsey and Cecil Patrick. We organized a hike to Sam Mack Meadow and beyond on Saturday 17 July.

3. CARMA observations of IRAS 19312+1950

Thomas Fok (University of Hong Kong) & Mislav Baloković (University of Split)

3.1. Introduction

IRAS 19312+1950 is an interesting object that has both properties of a young stellar object (a bipolar outflow) and an evolved star (an extended expanding envolope). It has been previously observed at millimeter wavelengths by Nakashima & Deguchi (2004), who have suggested that the interesting molecular emission line profiles and their spatial distributions arise from the complex structure of the star's environment. The aim of our observations was to investigate the connection between the its morphology and the molecular line profiles in order to better understand the structure of this object and its immediate neighbourhood.

3.2. Observations and Data Reduction

We have used CARMA in the E configuration during the nights of July 13 and 14. Our total observing time was 9 hours, with 6.8 hours on target. This was more than enough to obtain very good signal to noise ratio for all the molecular emission lines that we targeted and for a solid detection of the continuum as well. We have configured the correlator bands to have seven 62-MHz bands and one 500-MHz band, which provided velocity resolution of 0.4 km/s and 14.4 km/s respectively. The narrow bands were aimed at detecting ^{12}CO (J=1-0), ^{13}CO (J=1-0), C^{18}O (J=1-0), SO (J$_k$=3$_2$-2$_1$), HCCCN (12-11 and 11-10) and CN (1-0 J=3/2-1/2 F=5/2-3/2) lines, while the wide band was used for calibration and continuum detection. Due to a technical problem, the phase centers of the two tracks were slightly different: 19h33m24.4s, 19°56'54.8" for the first and 19h33m24.0s, 19°56'55.0" for the second one (both given in J2000.0 coordinates). We had to pay special attention to this fact in our data reduction because the MIRIAD software package automatically considers such an observation to be a two-pointing mosaic image. Data reduction was performed with MIRIAD and a general reduction script provided in the School.

3.3. Results, Discussion and Outlook

Our first result is that we have detected all the molecular lines that we aimed for. In the observation time given to this project even the weakest emission line achieved a signal-to-noise ratio in excess of 10. When plotting spectra, we binned two channels per bin, which further reduced S/N and gave us ∼0.8 km/s resolution. As expected from earlier observations, all lines were redshifted to the systemic velocity of the star, ∼37 km/s. In Figure 1 we show the spectral line profile and the integrated velocity map for the strongest detected line, the ^{12}CO (J=1-0). It is worth noting that the profile we observed is even richer in features than the one observed by Nakashima & Deguchi (2004), for example, in the weak apsorption features probably imprinted by the intervening interstellar medium.

CARMA E-configuration gave us just enought spatial resolution to marginally resolve some of the extended structure. As we detected all 7 molecular lines with high S/N, we were able to resolve their spatial dependence and associate some spatial features to the ones in the spectrum. This was achieved by plotting channel maps, similar to the ones in Figure 2. It can be clearly seen from the figure that the positional origin of the broad CO emission line component is quite different from the spatial distribution of the narrow-line emitting gas. We belive that this is a signature of the broad-line emitting expanding spherical shell and a directed, possibly biploar, outflow component which produces the narrow emission.

Although in this report we do not show the rest of the molecular emission lines and their channel maps, it is important to stress that they also seem to follow the broad/narrow line profile pattern displayed in channel maps for the CO line. Namely, lines ^{13}CO (J=1-0), C^{18}O (J=1-0), HCCCN(12-11) and HCCCN(11-10) appear to be narrow and emerge from a significantly elongated region in the NE-SW direction, while the SO (J_k=3_2-2_1) and CN (1-0 J=3/2-1/2 F=5/2-3/2) lines have broad components that emerge from the central region consistent with a point source, given the size of the E-array synthesized beam.

At last, in Figure 3 we plot two instances of what appear to be regions Doppler-shifted with respect to each other, for the ^{13}CO and the C^{18}O lines (more accurately, their shifted narrow components). In both cases the spatially-dependent Doppler shift hints at interesting properties of the moving gas around IRAS 19312+1950, but the details of its structure are just beyond the reach of the CARMA E-configuration. Therefore, in our future research of this object we will propose to image it at a higher resolution in order to be able to explore it in greater detail.

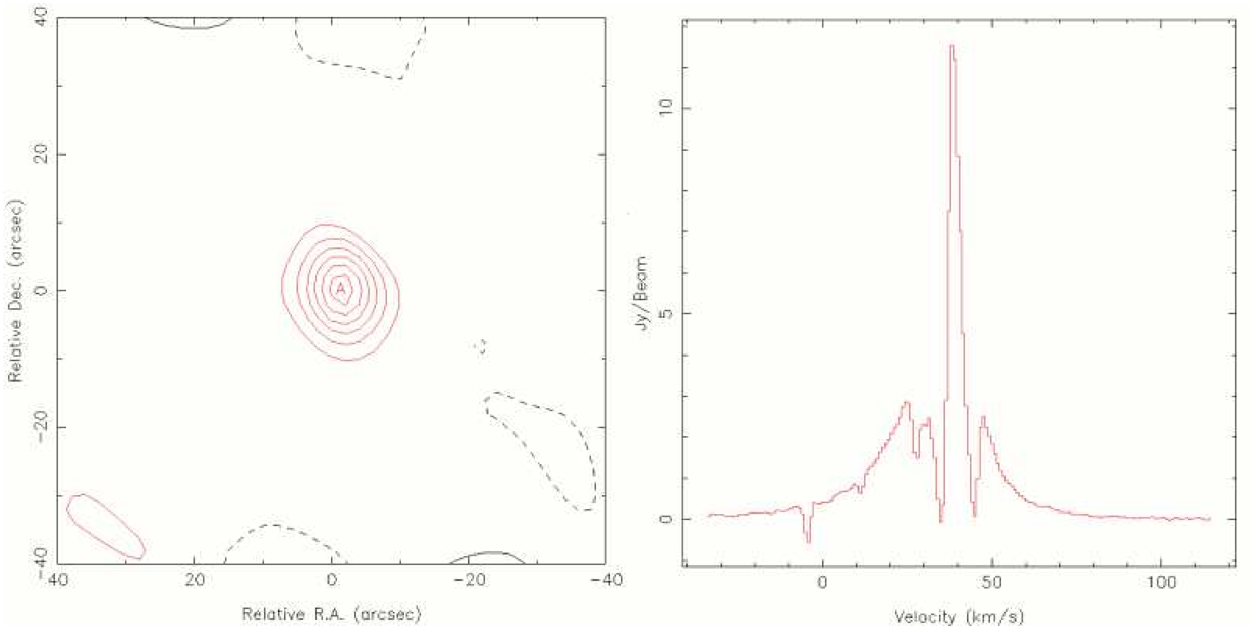

Fig. 1.— In the left panel of this image we display a high signal-to-noise integrated velocity map for the ^{12}CO line observed at the position of IRAS 19312+1950. The spectrum at the peak of the CO image is plotted in the right panel. Note the narrow and the broad components of the emission and the minor absorption features blueward of the emission peak.

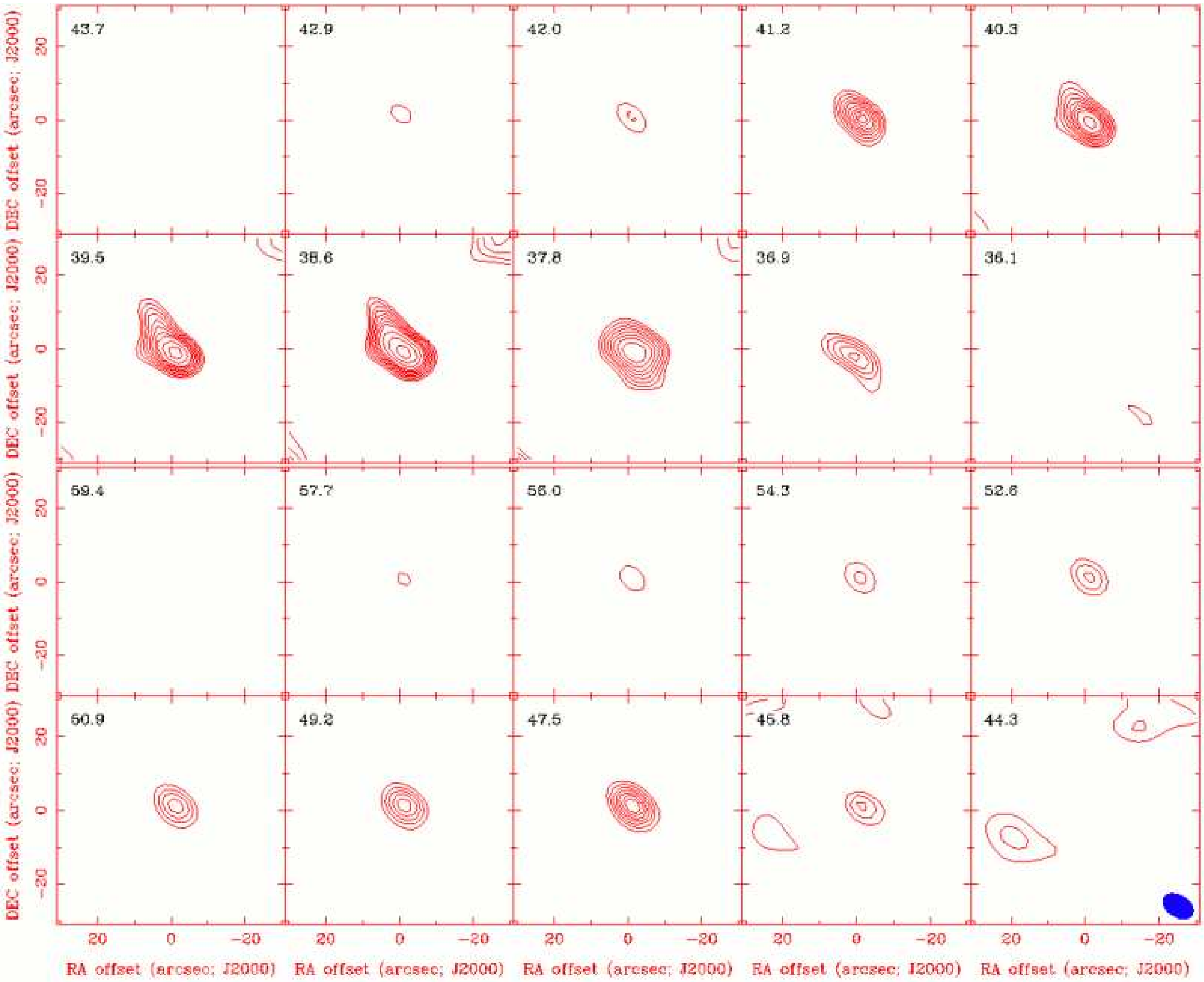

Fig. 2.— This figure shows channel maps for the CO line. The upper half (upper 8 frames) are channels where narrow emission line dominates, while the lower half are channels in which only broad emission is present. The numbers in the upper left of each frame display the mean velocity of the channel (refer to Fig. 1 for the line profile). The blue ellipse in the lower right matches the synthesized beam of the CARMA E-array. Note that the broad emission is consistent with a point source, while the narrow emission appears to be extended.

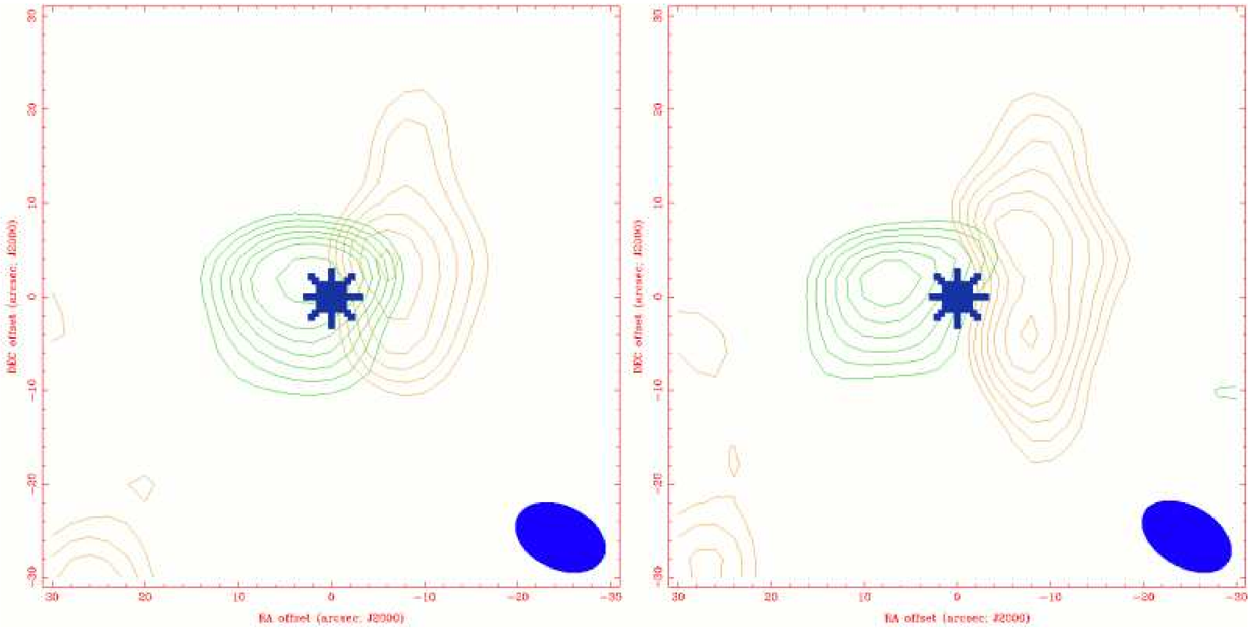

Fig. 3.— Both panels of this figure show velocity-separated emission seen in the ^{13}CO (left panel) and C^{18}O (right panel) lines. The orange contours correspond to emission integrated over the blue half of the lines, while the green contours mark the red half. The blue star marks the position of IRAS 19312+1950 and the ellipse shows the synthesized beam. Although there is a hint of a bipolar outflow from these plots, the spatial resolution of the observations is too low for investigation in greater detail.

4. Outflows in the Star Forming Region NGC1333

Swarnima Manohar (CIT) and Adele Plunkett (Yale)

NGC1333 is a star forming region in the Perseus cloud that contains numerous molecular outflows and shocked regions. Optical/near-IR surveys have studied the region's dusty pre-main-sequence population, and submillimeter continuum observations have identified low-mass protostars Sandell & Knee (2001). The region is shown in Figure 4, but even this large area $\sim 13' \times 18'$ does not cover all of the star formation activity.

It is an important project to observe the entirety of the region because the numerous outflows can affect other star formation in the region. Outflows inject energy and momentum into the surrounding cloud, accelerating and moving the surrounding dense gas. We observed one particular class I object, ASR 33, labeled in Figure 4. This object is located along a concentration of dust, between two strong continuum emission regions in the north and south. There are also cavities to the west and north of ASR 33, thought to be associated with its large outflows.

We observed the region of NGC1333 centered at RA=03:29:11.31 and Dec=+31:18:31.10 with a 19-point mosaic in a standard hexagonal pattern. We used 0336+323 as the phase calibrator and 3C84 as the gain calibrator. We observed for 4.6 hours on 14 July 2010, but our time was terminated by technical difficulties. We did, however, reduce the rest of our data from this observation during the following days of the school. We observed the same source for 3.8 hours on 16 July 2010 but due to inclement weather the data would not benefit our analysis. We hope to add data from a final 3 hours observed on 17 July 2010 to augment our current analysis.

We configured the bands such that the three major lines we wanted to observe (^{12}CO, ^{13}CO, C^{18}O) were in narrow bands. These three lines are an excellent way to map the molecular gas dynamics in the star-forming regions and would give us an insight into the structure of the outflows. ^{12}CO is optically thick and probes the outflow regions. ^{13}CO is optically thin and probes the central regions near a protostar. C^{18}O probes the ambient medium. Unfortunately, we lost the use of the band to detect C^{18}O.

Ten 500 MHz bands were used to detect continuum emission in the region. However, one of the bands had the CO emission line in it, so we removed it from consideration. We also removed some other bands because we suspected some other lines were present that contaminated the continuum data. Figure 5 shows the continuum emission from the region detected with five wide bands. Although it is hard to say that this is definitely continuum emission, the image indicates that there may be some emission in the region; further analysis will confirm the continuum emission.

The ^{12}CO emission showed a different structure from the continuum. Figure 6 shows ^{12}CO in this region, and the side panel shows the gradation in Jy. Only the middle 80 channels were used for this image to eliminate as much of the noise as possible and concentrate only on the line. As can be seen by comparing the continuum image and the CO emission line image, the structures are not centered around the same point. We detected a signal to noise ratio of about 10 in this image. The velocity ranges from 10 to 35 km/s in different parts of the observed region. Figure 7 shows different regions that showed CO emission with different velocity cuts to break down the gas dynamics in the region. The extended regions in the map indicate outflows from the central star forming region. Spectra also show the characteristic shape to indicate outflows.

Figure 8 shows the region in ^{13}CO emission and the side panel shows the gradation in Jy. Only the middle 80 channels were used to reduce noise, as most of the line emission was concentrated in those channels. This image shows emission in a region similar to the continuum region. It might indicate a higher concentration of molecular gas in that region, while ^{12}CO emission traces the more extended and less concentrated molecular gas. As for ^{12}CO emission before (Figure 6), we generated velocity maps for the ^{13}CO emission. There was much less structure detected in ^{13}CO as in ^{12}CO; outflows from the central region are mostly seen in the ^{12}CO emission line map.

Combining the information from the continuum, ^{12}CO, and ^{13}CO emission line maps indicates outflows in this star forming region in NGC 1333. We need to clean the already reduced data further and take more extensive observations of the region in other lines to have clearer evidence of outflows. Also, the addition of the C^{18}O line map would give us a better picture of the gas dynamics of the region, as well as enable the measurement of other ambient cloud properties including mass, momentum, and energy.

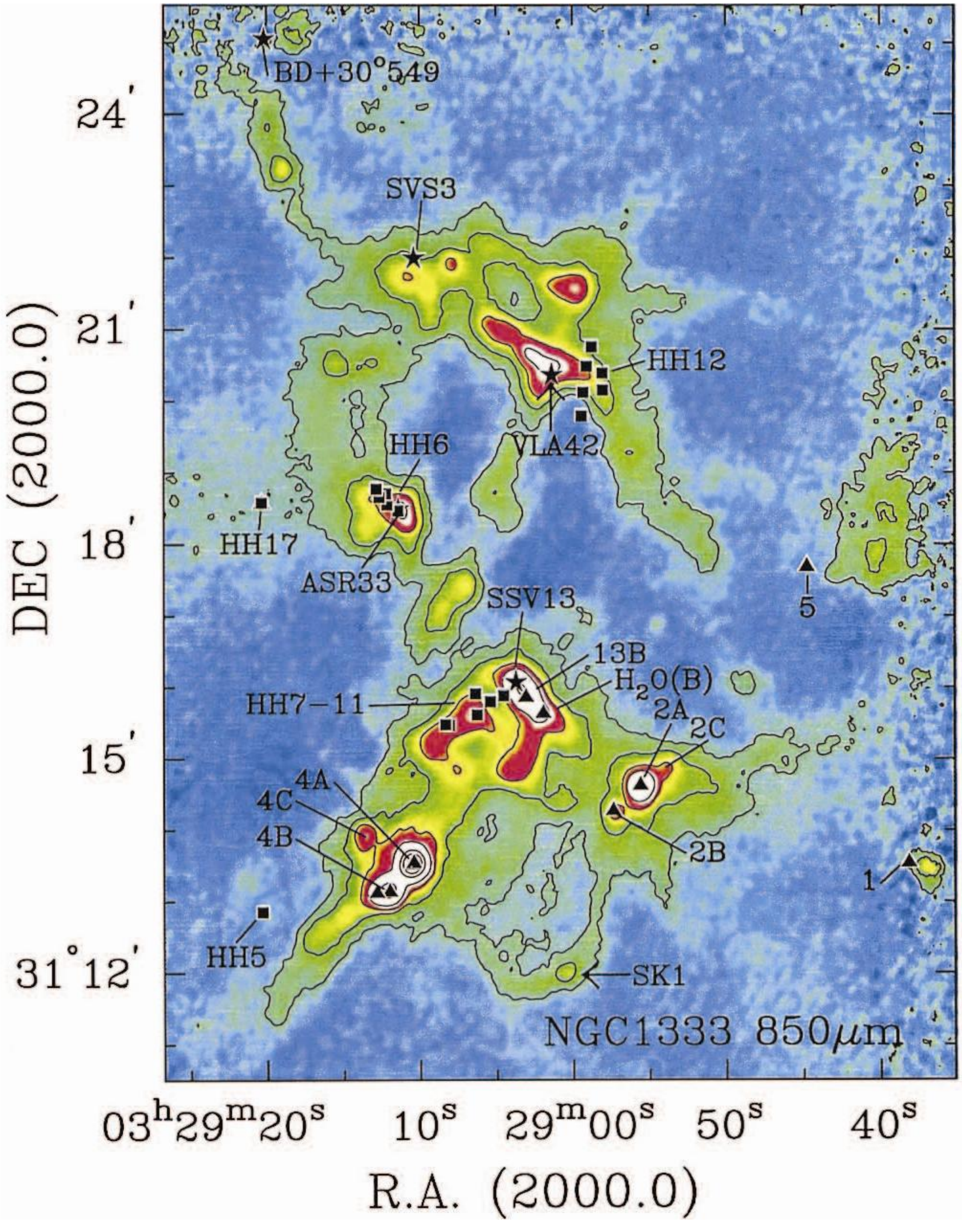

Fig. 4.— NGC1333 region, shown in 850 μm Sandell & Knee (2001). Filled squares are HH objects, filled stars are pre-main-sequence stars, and filled triangles are IRAS sources or known protostars. We observed an area $\sim 3' \times 3'$ centered at ASR 33.

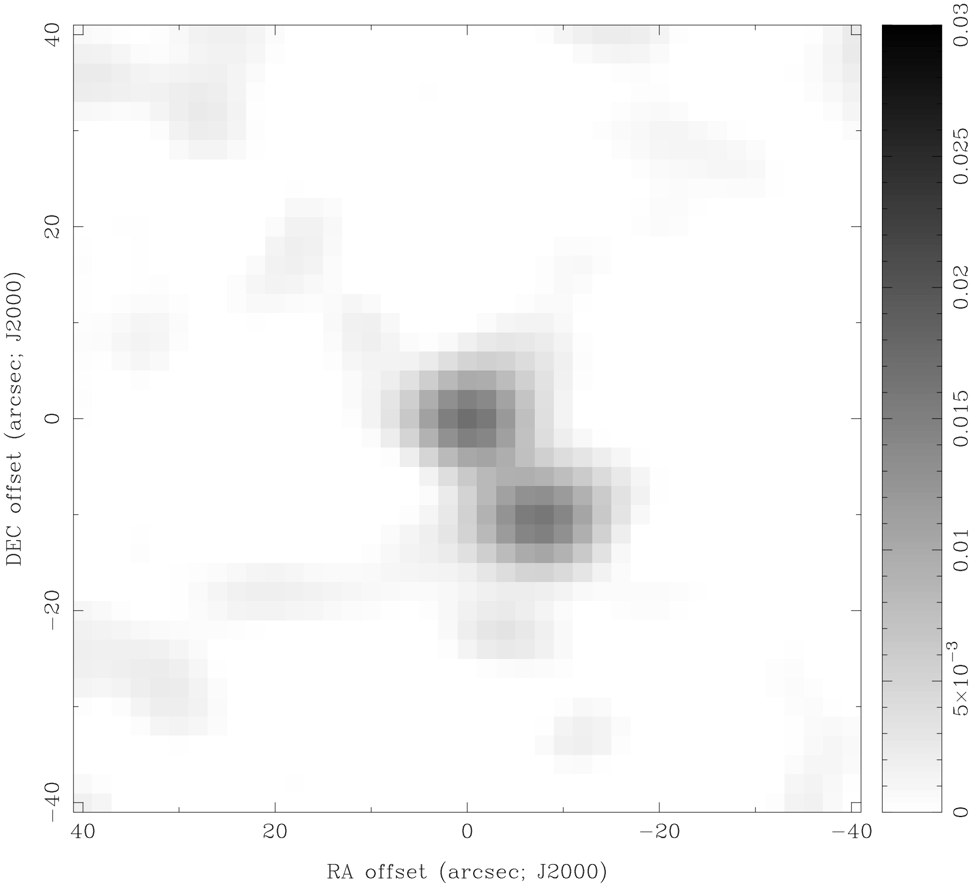

Fig. 5.— Continuum emission image of the region observed in NGC1333 based on data from 5 wide bands

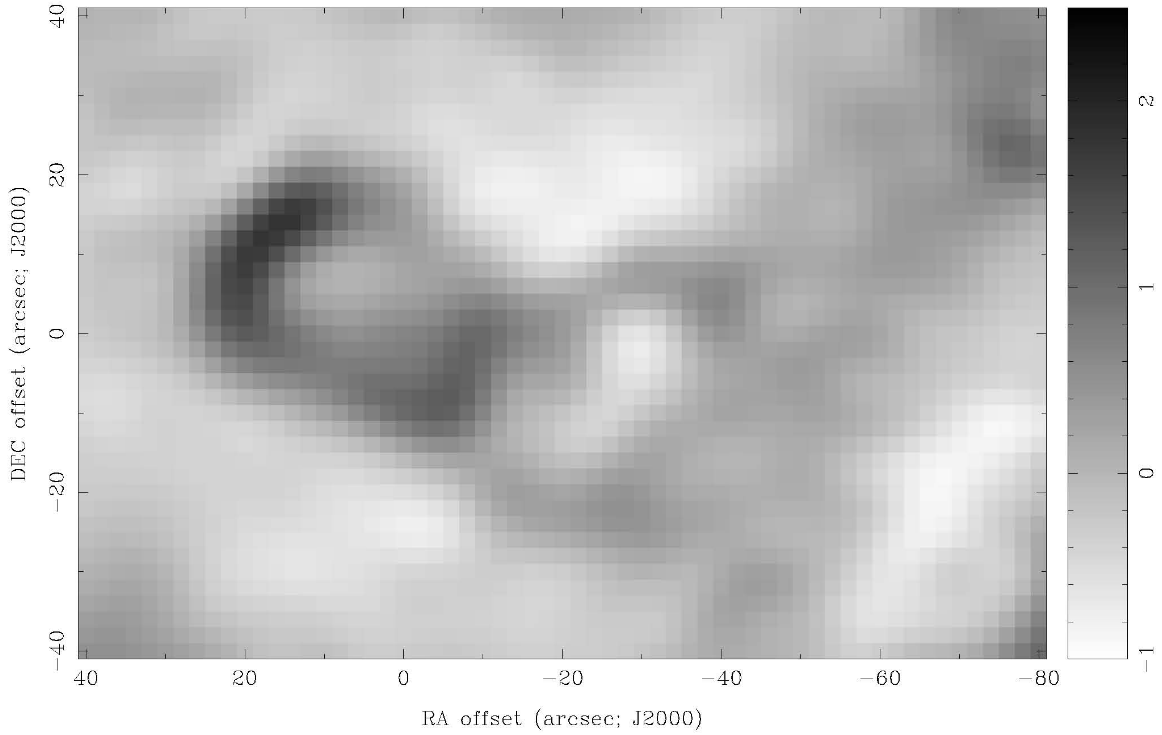

Fig. 6.— Star forming region in NGC1333 observed in ^{12}CO. Only 80 center channels were used to make the above image to reduce noise. This was a 10 sigma detection.

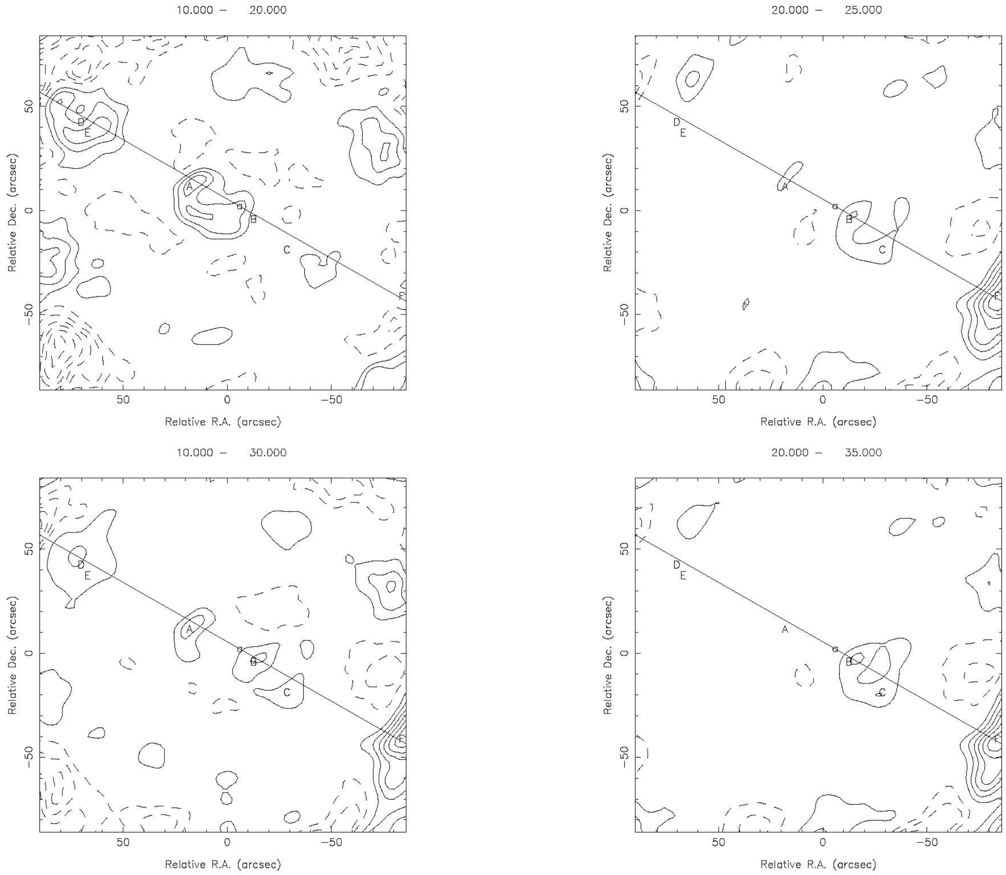

Fig. 7.— Star forming region in NGC1333 observed in ^{12}CO. The image shows the different regions with velocity cuts for 4 different velocity ranges to show gas dynamics of the area.

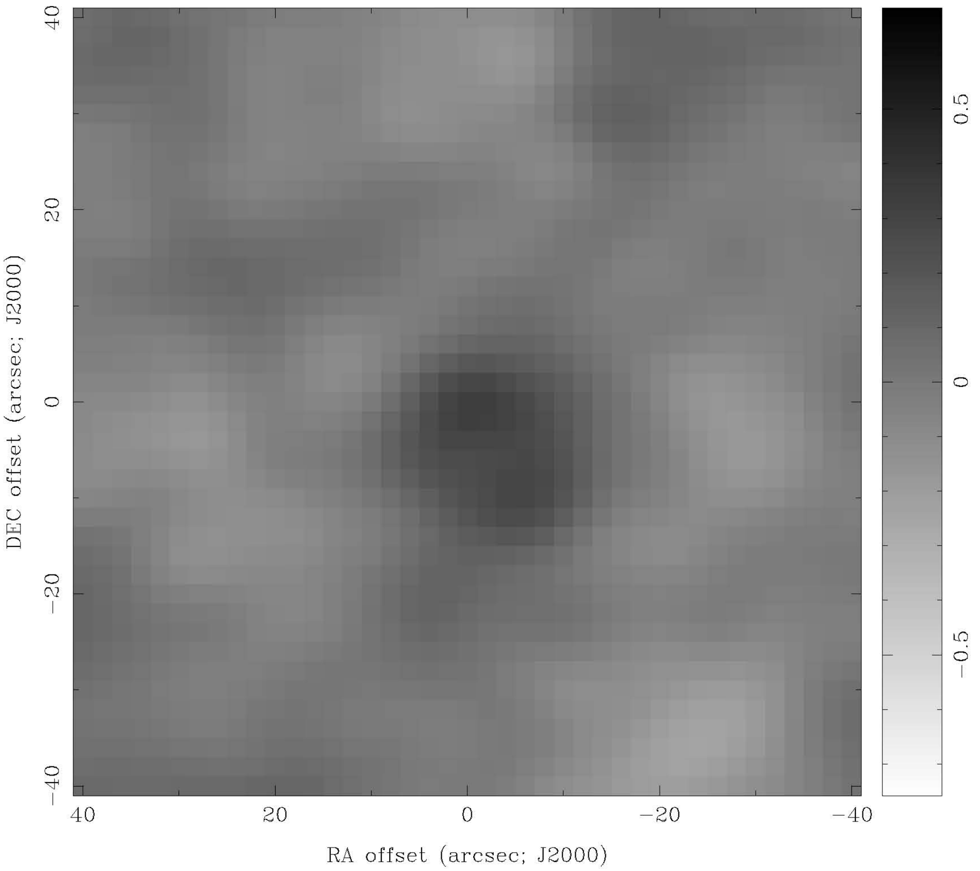

Fig. 8.— Star forming region in NGC1333 observed in ^{13}CO. Only 80 center channels were used to make the above image to reduce noise. This was a 8 sigma detection

5. APEX-SZ: SZ Cluster Science and Point Source Contamination

Benjamin Westbrook (University of California, Berkeley), Felipe Navarrete (MPIfR, Bonn, Germany)

5.1. Introduction

The APEX-SZ instrument is a millimeter-wave cryogenic receiver designed to observe galaxy clusters via the Sunyaev-Zel'dovich effect (SZ; Sunyaev & Zeldovich 1970) from the 12 m APEX telescope on the Atacama plateau in Chile. The receiver contains a focal plane of 280 superconducting transition-edge sensor (TES) bolometers instrumented with a frequency-domain multiplexed readout system. APEX-SZ observes in a single frequency band at 150 GHz with 1' angular resolution and a 22' field-of-view, all well suited for cluster mapping. Since its commissioning in April 2007, APEX-SZ has been used to map tens of clusters.

Observation of clusters is done at 150 GHz where the decrement of the SZ signal is maximum. In the absence of point sources contributing flux at 150 GHz, the cluster's SZ signature is a deficit of photons that produce a spectral distortion of the Cosmic Microwave Background (CMB) black body radiation. If a point source contributes a significant amount of flux at 150 GHz, characterization of a galaxy cluster via the SZ effect can be compromised and in some cases untenable. At 150 GHz, astronomical data suggest that both bright radio sources and dusty IR galaxies can have significant emission at 150 GHz (Knox et al. 2004; Lin & Mohr 2007; Lin et al. 2009).

The CARMA instrument is well suited to check for point sources that could alter the SZ signature of clusters which have either already been measured by APEX-SZ or ones we wish to measure in the future. In particular, it's ability to measure flux in the 90 GHz band can be used to check for radio point sources while the 230 GHz band can be used to check for dusty IR sources.

Table 1: Summary of APEX-SZ cluster Positions Observed with CARMA with detections integrated to sufficient noise levels 90 GHz.

Target Name	Pointing (RA, DEC)	[a] Expected Flux	[b] Peak Flux ± σ (S/N)	Time on source
–	(J2000,J2000)	mJy	mJy/beam	min
A2390	(21:53:36.82 , 17:41:43.63)	12.76	21 ±1.7 (12σ)	33.5
A2537A	(23:08:28.39 , -2:02:36.76)	3.79	5.2 ± 1.1(4.8σ)	60
RXJ1504A	(15:04:07.50 , -2:48:16.58)	3.28	7.4 ± 0.83 (8.9σ)	60

---

[a] NVSS flux at 1.4 GHz is extrapolated to 90 GHz assuming an spectral index value of $\eta = -0.7$

[b] S/N refers to signal-to-noise ratio

Table 2: Summary of APEX-SZ cluster positions observed with CARMA with non-detections integrated to sufficient noise levels 90 GHz.

Target Name	Pointing (RA, DEC)	[a] Expected Flux	[b] Peak Flux ± σ (S/N)	[c] Upper Limit	Time on source
–	(J2000,J2000)	mJy	mJy/beam	mJy/beam	min
A520A	(4:54:01.20 , 2:57:46.51)	0.34	±1.0	3.00	60
A1689A	(13:11:31.50 , -1:19:29.19)	3.23	±1.5	4.50	30
RXJ1504B	(15:03:43.70 , -2:50:15.39)	0.33	±1.6	4.8	60
XMM2215	(22:15:59.50 , -17:38:02.99)	—	±1.5	4.5	45
Zw3146	(10:23:45.09 , +04:10:40.7)	5.19	-3.0 ± 0.98 (-3.0σ)	2.9	32.5

---

[a] NVSS flux at 1.4 GHz is extrapolated to 90 GHz assuming an spectral index value of $\eta = -0.7$

[b] S/N is the signal-to-noise ratio

[c] This is the 3σ value

Table 3: Summary of APEX-SZ cluster positions observed with CARMA with non-detections integrated to insufficient noise levels 90 GHz.

Target Name	Pointing (RA, DEC)	[a] Expected Flux	[b] Peak Flux ± σ(S/N)	[c] Upper Limit	Time on source
–	(J2000,J2000)	mJy	mJy/beam	mJy/beam	min
A520B	(4:54:20.80 , 2:54:58.71)	1.43	± 260	780.00	60
A2537B	(23:08:05.50 , -2:13:53.69)	0.18	±3.1	9.30	11
RCS2319	(23:19:54.00 , 0:38:00.01)	—	±160	480.00	15
A1835	(14:01:2.05 , +02:52:41.0)	2.13	1.2 ± 0.32 (3.5σ)	0.96	120

---

[a] NVSS flux at 1.4 GHz is extrapolated to 90 GHz assuming an spectral index value of $\eta = -0.7$

[b] S/N is the signal-to-noise ratio

[c] This is the 3σ value

5.2. Clusters - Observations Done at CARMA

APEX-SZ has mapped the SZ signature of tens of clusters. Cluster selection is based on X-Ray temperature, previous and current research on the source, point source catalogs, dynamical state and several other criteria. Some of these clusters have bright NVSS (1.4 GHz) point sources within 2 arcmins of the X-Ray cluster center, which was the primary selection criteria for observations done at CARMA. In addition we observed the position of XMMJ1230, which we do not detect in the SZ despite the fact that it is a hot X-Ray source.

Although the NVSS catalog is a comprehensive all sky survey at 1.4 GHz, it does not provide a comprehensive reference for all point sources which could contaminate a cluster's SZ signature at 150 GHz. Radio point sources with significant detections at 1.4 GHz could potentially have rising or flat spectra and could possibly be emitting at 150 GHz. Furthermore, observations at 1.4 GHz do not probe dusty IR sources which can also contribute flux at 150 GHz. Currently, there does not exist comprehensive point source surveys at 90 or 230 GHz (Sadler et al. 2008; Lin et al. 2009). The CARMA instrument is well suited to measure and understand potential point source contamination of SZ signals. To date, the APEX-SZ collaboration has observed the positions of 9 X-Ray cluster centers with the CARMA instrument. Tables 1, 2, and 3 summarize the results of CARMA observation of clusters observed with APEX-SZ.

5.2.1. Selection criteria

We first check for NVSS sources with flux greater than 10 mJy (at 1.4 GHz) within 2 arcminutes from the X-ray cluster center. Radio sources that fit this criterion were found for all but one of the clusters we observed with CARMA (Condon et al. 1998). We then estimate the required rms level of our observations, by extrapolating the NVSS flux at 1.4 GHz to 90 GHz assuming an spectral index of $\eta = -0.7$ (where, the spectral index η id defined by $S_\nu \propto \nu^\eta$), which is typical value for synchrotron radiation (Condon 1992). Although this method gives an estimate of the flux at 90 GHz, we expect large discrepancies between the extrapolated flux and the actual flux value for two reasons. Due to the lack of data we have to assume that all radio sources are falling spectra with a spectral index of $\eta = -0.7$, so any flat or rising sources will have a flux much greater than this extrapolated value. Furthermore, even if the spectral index of $\eta = -0.7$ is valid near 1.4 GHz, there is no a priori reason that it should be valid over two order of magnitudes in frequency.

5.2.2. Observation Strategy and Data Reduction

All of the observations at CARMA were taken at 90 GHz in continuum mode covering a 8 GHz bandwidth centered on the observation frequency. In addition we also observed one cluster in continuum mode at 230 GHz. Continuum observation is well suited for our purposes as we expect that point source contamination that could compromise the SZ will have continuous emission spectra. Furthermore, we do not expect spectral lines to contribute significant flux at 150 GHz.

Continuum observation also simplify the data reduction process. In all of the reductions below a very similar filter and flagging set was used for all observation. In all cases bad antennas, shadowed baselines, high elevation data baseline, edge channels were flagged. After flagging is done, we applied baseline and line length calibration to the data. The data is then flux calibrated and then a final calibration is done on the amplitude and phase. The images are inverted and cleaned using natural weighting (i.e. robust=2) to maximize sensitivity. The statistics of these observations are reported in Tables 1, 2, and 3.

5.2.3. Abell 2390

As a demonstration of the method, we present the strong detection of a source at the position of the cluster A2390. This point source shows a flux density of 215 mJy at 1.4 GHz in the NVSS catalog. In Figure 9 we show the detection of the point source at 90 GHz with a flux density of 21 mJy and a map rms of 1.7 mJy/beam. We have decided to discontinue observing this cluster because of this point source.

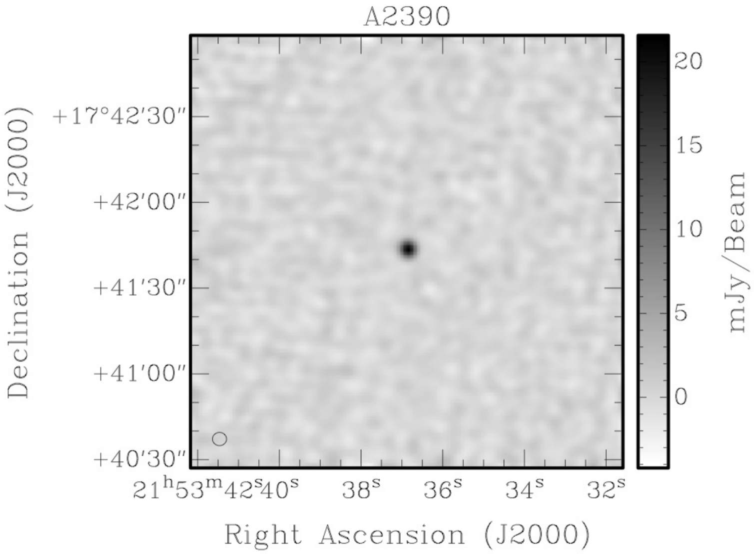

Fig. 9.— Map of point source observed at the position of the Galaxy cluster Abell 2390. This map has an rms noise of 1.7 mJy/beam and the source has a flux of 21 mJy at 90 GHz. This observation is consistent with the 215 mJy detection of the same source at 1.4 GHz.

5.2.4. XMMJ1230

APEX-SZ has observed the high redshift ($z = 0.965$), massive X-ray detected cluster XMMJ1230 cluster in attempt to measure its SZ decrement at 150 GHz. Although the X-ray data suggest that the temperature of the cluster is 6 keV and we predict a decrement of -215 μK CMB, we measured a null decrement after more than 25 hours of observations $-3 \pm\ 60\ \mu K_{CMB}$; this is a 3 sigma discrepancy with the X-ray data. We hypothesize that this discrepancy with the X-ray data is due to either a radio source or a dusty IR galaxy. We calculate a 10 mJy source at 150 GHz would be sufficient to explain our non-detection. However, data taken during the 2010 summer school suggest that there are no radio sources with signifcant emission at 90 GHz present at this location. Figure 10 shows the 90 GHz map of the source position of XMMJ1230. No significant point sources are detected at 90 GHz suggesting that if the SZ signal is being cancelled by a point source, the source must be a dusty source whose intensity peaks at or above 150 GHz. We attempted to observe the source at 230 GHz as well. However, the weather was so bad that the 230 GHz data are unusable. Follow up observation needs to be done on this cluster at 230 GHz with improved weather conditions.

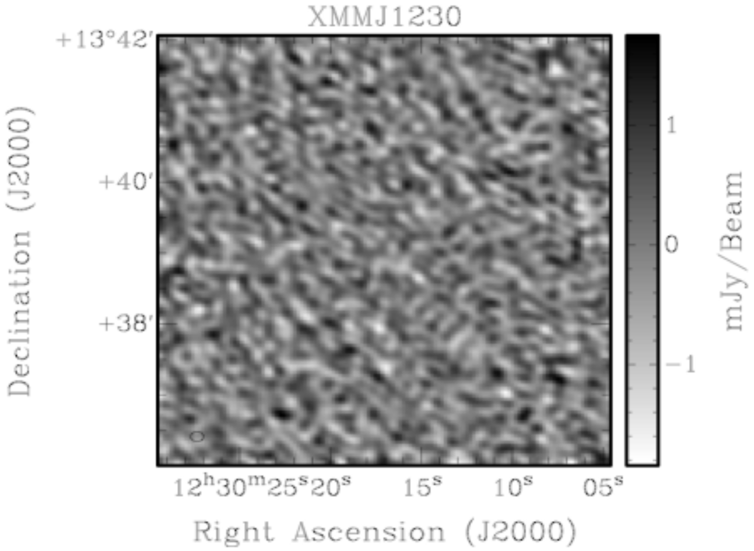

Fig. 10.— A 90 GHz map of the position of the Galaxy cluster XMMJ 1230. This map has an rms noise of 0.4 mJy/beam with no detection. This observation is inconsistent with a point source providing 10 mJy of flux at 150 GHz, which is needed to explain the non-detection of the cluster. A follow-up observation at 230 GHz is necessary.

5.2.5. Abell 1835

This cluster has an identified radio source at 1.4 GHz offset 69" from the X-ray cluster center; a flux of ~ 2 mJy is expected at 90 GHz. At this position a marginal detection of 1.15 mJy ($\sim 3.5\sigma$) is found. To confirm this as a real detection more integration time would be needed. The results are shown in Table 2 and in the left column of Figure 11. The signal-to-noise ratio has been calculated using the values from the central pixel of the signal and rms map.

5.2.6. Zw3146

This cluster has an identified radio source at 1.4 GHz offset 87.2" from the X-ray cluster center; using a spectral index of $\eta = -0.7$ a flux of 5 mJy is expected at 90 GHz. However, no significant detection is found at this position. The results are shown in Table 2 and in the right column of Figure 11.

5.3. Conclusions

SZ science is one of the best tools scientists have to study the structure of galaxy clusters and thus the Large Scale Structure of the universe. Accurate measurements of many clusters in the SZ will provide valuable information which can be used to constrain cosmological parameters and uncover the details of cluster dynamics. Understanding point sources is crucial to understanding SZ decrements and the physics behind galaxy clusters. Combining data from experiments like APEX-SZ and CARMA provide a unique and comprehensive way of studying galaxy clusters at mutliple frequencies and with different resolution. Combined data sets like this will provide the basis for future studies of point sources, galaxy clusters, and cosmology.

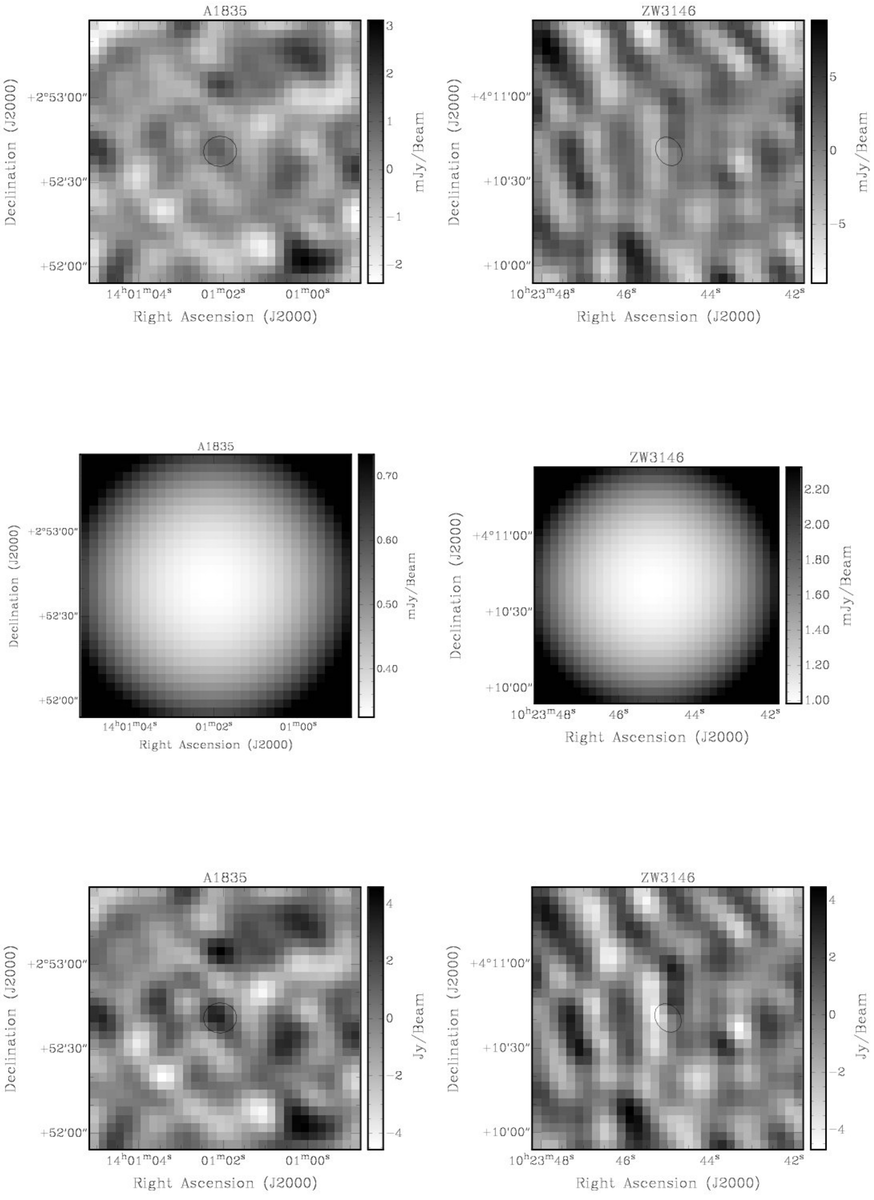

Fig. 11.— Reduced images of A1835 and Zw3146. Top row: The signal map. Middle row: The rms noise map. Bottom row: The signal-to-noise map. The synthesized beam is overlaid in the center of the image.

6. Finding the Unseen Molecular Gas Inside the Inner Linblad Resonance

Katie Jameson & Rodrigo Herrera Camus (University of Maryland)

6.1. Introduction

In the last two decades, our knowledge of the average properties of the gas in the inner 400 pc of the Galaxy has been improved thanks to surveys mapping ^{12}CO (Bally et al. 1987) and HCN (Lee 1996) among others. Today, we know that at least one stellar bar crosses the Galaxy, and the x_1 and x_2 orbit families resulting from its potential contain atomic and molecular gas respectively (Binney et al. 1991). In theory, the atomic gas in the x_1 orbit is slowly torqued by the bar and fall inwards, reaching the inner Lindblad resonance where it shocks and may form molecular gas that will eventually join the x_2 disk. However, many questions regarding the gas clumps falling to the x_2 disk remains. What is the typical density and size of these clumps? What is the mass transfer rate between the atomic and the molecular ring?. So far, single dish molecular surveys have failed detecting and characterizing the gas content that lyes between rings. The main reason behind these non-detections seems to be resolution: in a large beam, if the clumps are small and far between, the low filling factor will make it impossible to see them. With a small beam, it takes forever to survey the region. This is why CARMA seems to be an ideal instrument for detecting this “hidden” clumps. In fact, Hodges–Kluck et al. (2009) found a significant number of small ($\sim$ 1 pc), dense ($\sim 10^5$ cm^{-3}) clumps using the CARMA D+E array configuration.

6.2. Science Goals

Having observed an empty region seen in the large–scale ^{12}CO and HCN surveys of the Galactic Center Ring, our goal is to find the missing mass neglected by previous surveys and characterize the molecular gas in this region.

6.3. Observations

We used the compact E-array configuration to observe an “empty” field in the galactic center located at R.A. $= 17:44:45$ and Dec $= -29:31:15$ (J2000). The track was 4.8 hr. long, with 3.6 hr. of integration time over the source. We used a 37-point mosaic that covered a region of approximately 3 arcsec in diameter. The correlator was set to observe HCN, HCO+, CS and SiO lines using narrow 125 Mhz windows and four wide 500 MHz windows to observe 3 mm continuum for calibration purposes.

6.4. Results

We detect HCN $(1-0)$, HCO$^+(1-0)$, and CS $(1-0)$ in the void region from $25-125$ km s^{-1}seen in the velocity–longitue $(l-v)$ maps of ^{12}CO from Bally et al. (1987) and HCN $(1-0)$ from Lee (1996). There were numerous clumps within the integrated spectral line images, consistent with what was found by Hodges–Kluck et al. (2009). We labeled the clumps that were identified by eye in each image and include the integrated spectra for each clump center. In Figure 12 there are four clumps identenfied in the HCN image and labeled A – D with the integrated spectrum at each point shown. The integrated spectrum shows that the emission is at velocities within the void region. Also, there is no strong emission from the velocities where there is strong emission in the large–scale maps (Bally et al. 1987), which is a product of only being sensitive to the small–scale features in the E array. Figures 13 and 14 show the same for the HCO$^+(1-0)$ and CS $(1-0)$ lines respectively with almost all (except clump B in the CS image) corresponding to emission from the void region.

6.5. Discussion & Conclusions

The detection of new clumps of molecular gas withing the galactic center region supports the work started by Hodges–Kluck et al. (2009) and shows that there is missing gas from the large–scale surveys and that these "voids" are not actually empty. Figure 15 shows integrated images for HCO$^+$ and CS with HCN contours overlaid. There is clearly some structure shown by combining the information from the different emission lines. We see that CS emission tends to trace the HCN peaks, whereas HCO$^+$ seems to be present along one edge of the HCN emission.

Although these molecular gas clumps were missed by the larger scale surveys towards the galactic center, this does not mean that they represent a negligible amount of mass. The presence of these molecular lines indicate that there is dense gas present. Typical observed line widths of HCN and HCO$^+$ are $10-20$ km s^{-1}, and with the size of these clumps being $\sim$ 1pc produces a virial mass estimate of $M_{vir} \sim 2 \times 10^4 M_\odot$, which is consistent with what was observed in a similar void previously by Hodges–Kluck et al. (2009). In this one void, there could be of order $10^5 M_\odot$present that was previously unaccounted for in the large–scale surveys.

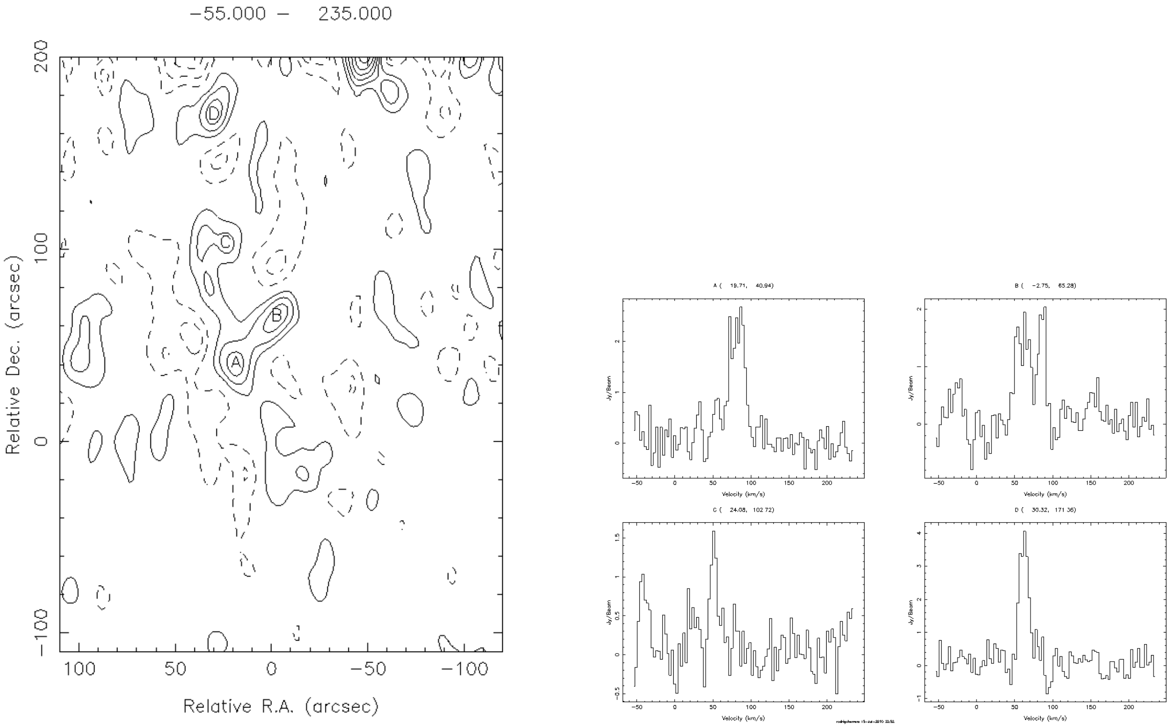

Fig. 12.— Left: Map of HCN(1 − 0) intregrated intensity from $v_{LSR} = -55 - 235$ km $s^{-1}$for the observed region at $l = -0.16$, $b = -0.14$. The peaks are labeled A through E. Right: Integrated spectrum of HCN for the peaks A–D in the observed region.

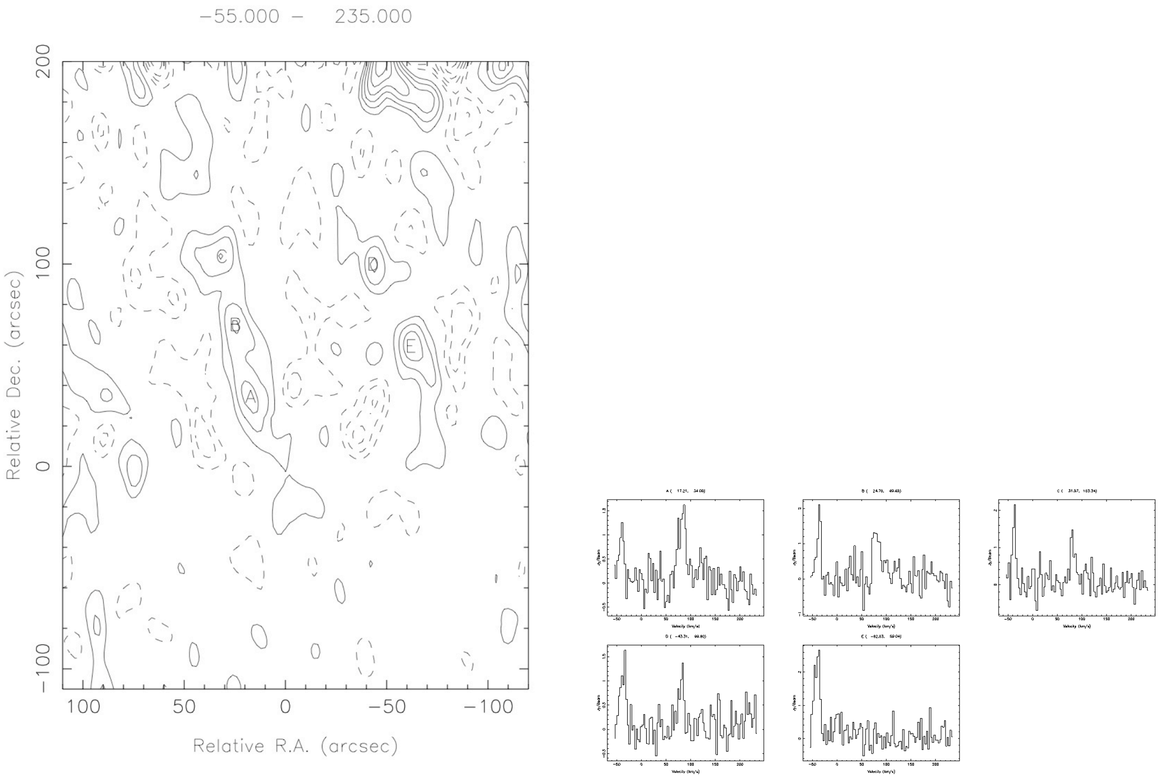

Fig. 13.— Left: Map of $HCO^+(1-0)$ intregrated intensity from $v_{LSR} = -55 - 235$ km $s^{-1}$for the observed region at $l = -0.16$, $b = -0.14$. The peaks are labeled A through E. Right: Integrated spectrum of HCO^+ for the peaks A-D in the observed region.

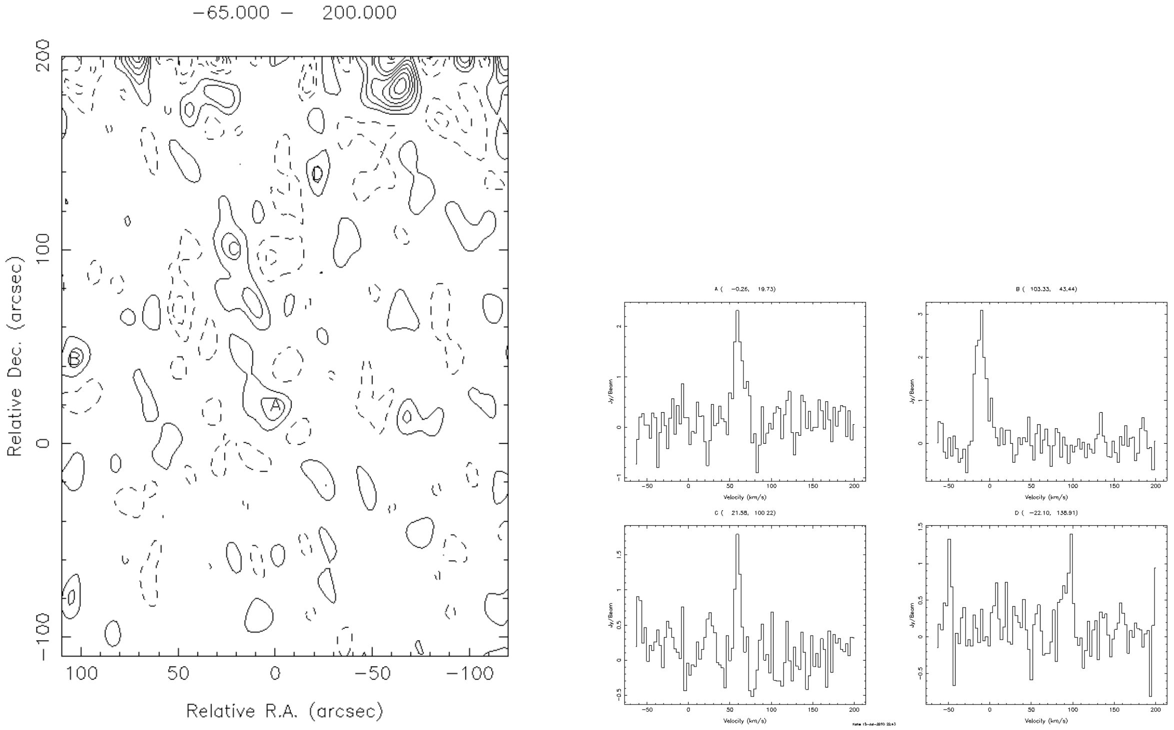

Fig. 14.— Left: Map of CS (1-0) intregrated intensity from $\mathrm{v}_{LSR} = -65 - 200$ km $\mathrm{s}^{-1}$for the observed region at $l = -0.16$, $b = -0.14$. The peaks are labeled A through E. Right: Integrated spectrum of HCO^{+} for the peaks A-D in the observed region.

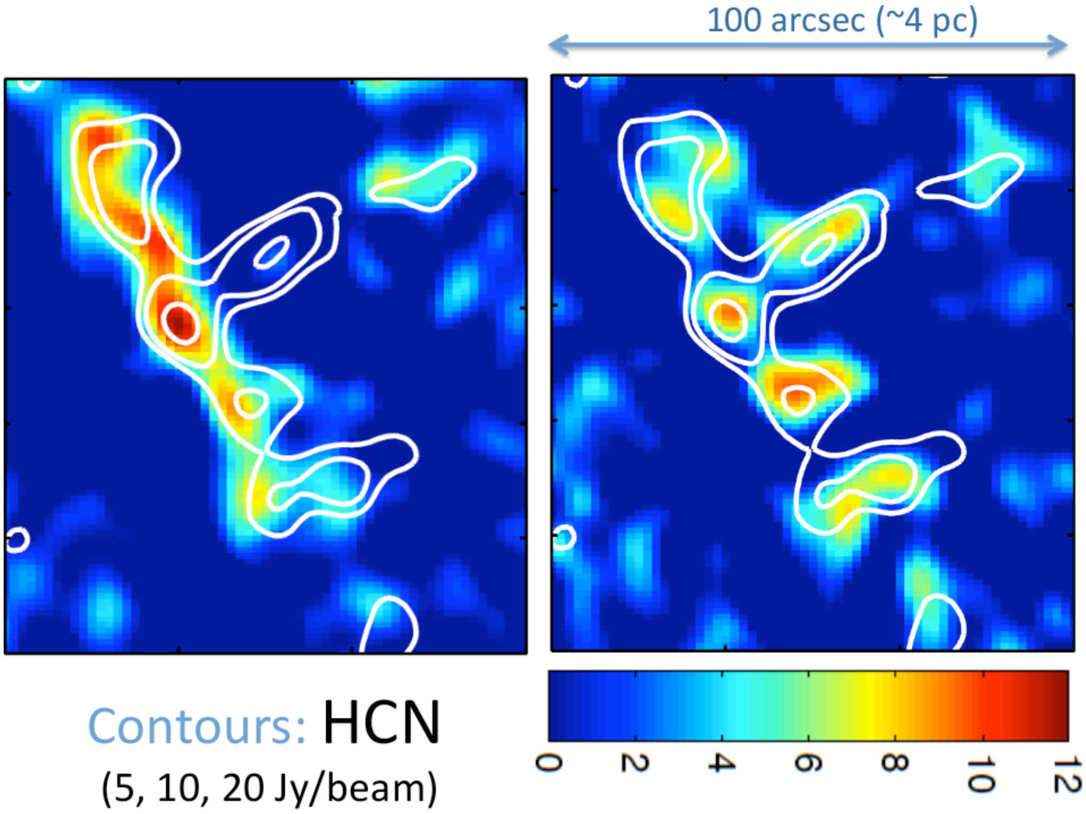

Fig. 15.— Integrated images of HCO$^+$ (left) and CS (right) with contours of HCN overlaid.

7. CO Observations of NGC 3627

Jason Speights, Thiago Goncalves, Tim Weinzirl, & David Fisher

The purpose of our project was to observe the 12 CO J = 1 - 0 line (ν_{rest} = 115.27 GHz) in the barred spiral galaxy NGC 3627. This galaxy was chosen for observation because: 1.) its moderate size and inclination make it easy to distinguish its barred and spiral structure; and 2.) flux measurements useful for estimating integration times were readily available from the BIMA SONG survey. The observations were made using a channel width of 3.5 km s^{-1}, and consisted of multiple fields within the central $2'$. The fields were combined and reduced in MIRIAD to make moment 0 maps that showed the nucleus, the bar, and the beginnings of the spiral arms.

Figure 16 shows how much of the galaxy was detected by the observations. In the figure is a contour map of the signal-to-noise overlaid on a 2MASS H-band image. The signal extending from the center out to the beginning of the spiral arms is most likely a real detection. The rest of the signal beyond the spiral arms is most likely an artifact of the deconvolution process. A substantial portion of the galaxy's structure, however, is detected in CO by the observations.

Figures 17 and 18 show moment 0 maps made using two different deconvolution methods. The map shown in Figure 17 was made using MOSSDI, which is a version of CLEAN for multiple field deconvolution. The map shown in Figure 18 was made using MOSMEM, which is a version of the maximum entropy algorithm, MAXEN, also for multiple field deconvolution. Both maps were made with a FWHM of $10.0''$ x $7.4''$ for the synthesized beam and a pixel size of $2''$. The RMS noise in a line-free channel was 215 mJy for the map in Figure 17, and it was 265 mJy for the map in Figure 18. CO is clearly detected in the nucleus and at the ends of the bar in both maps. The distribution of CO along the bar and at the beginnings of the spiral arms is more clearly defined in Figure 18 than it is in Figure 17.

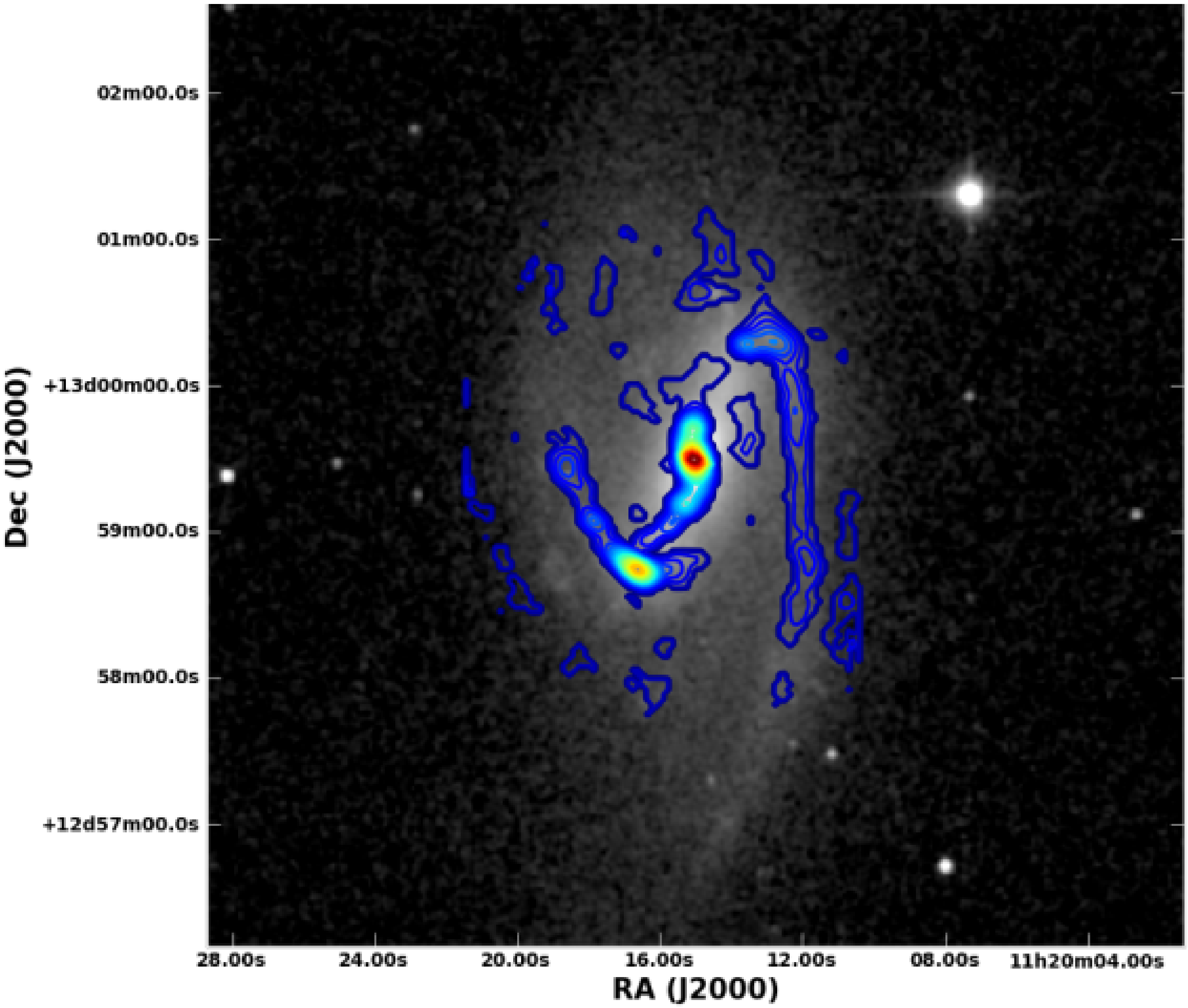

Fig. 16.— Contour map of the signal-to-noise overlaid on the 2MASS H-band image. The contour levels range from ∼120 in the galaxy center to ∼20 in the spiral arms.

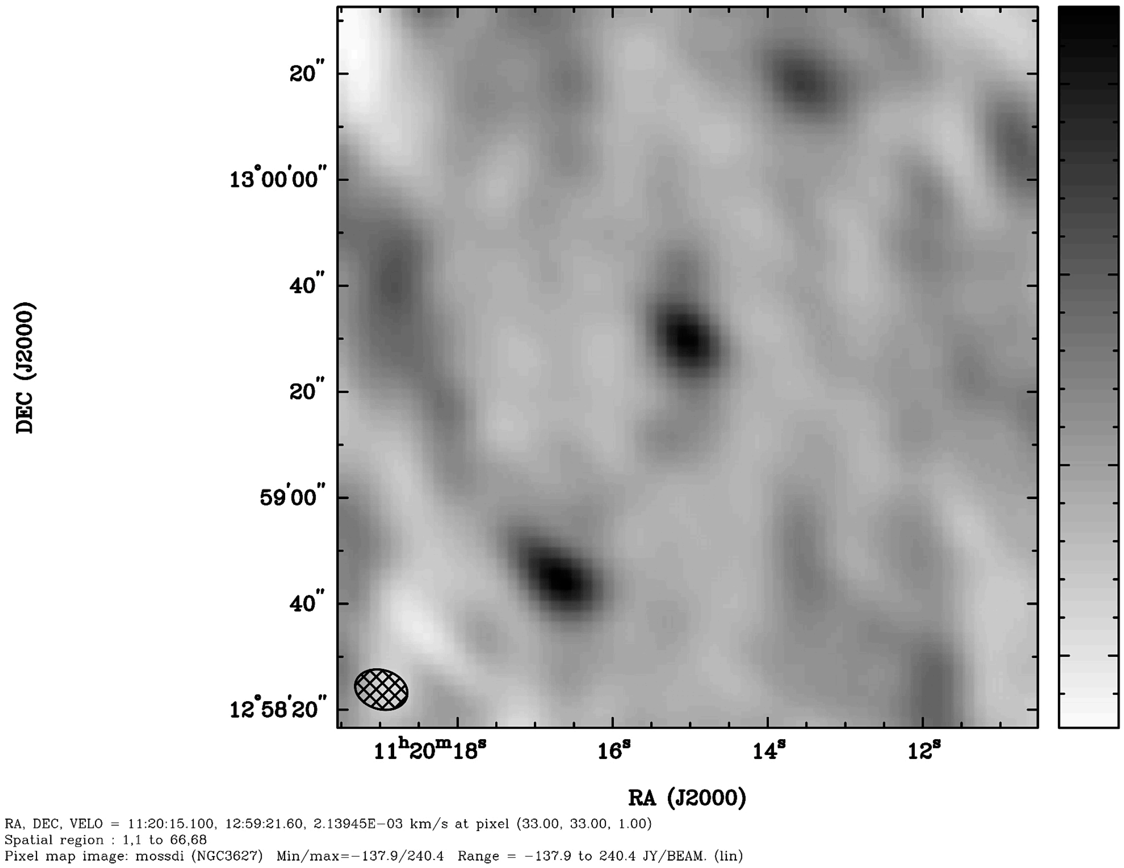

Fig. 17.— Moment 0 map made using MOSSDI. Note the large fluctuations in the intensity. The CO in the nucleus is clearly seen in the center of the map. The other two bright spots are located at the ends of the bar. The distribution of CO along the bar and spiral arms is poorly defined.

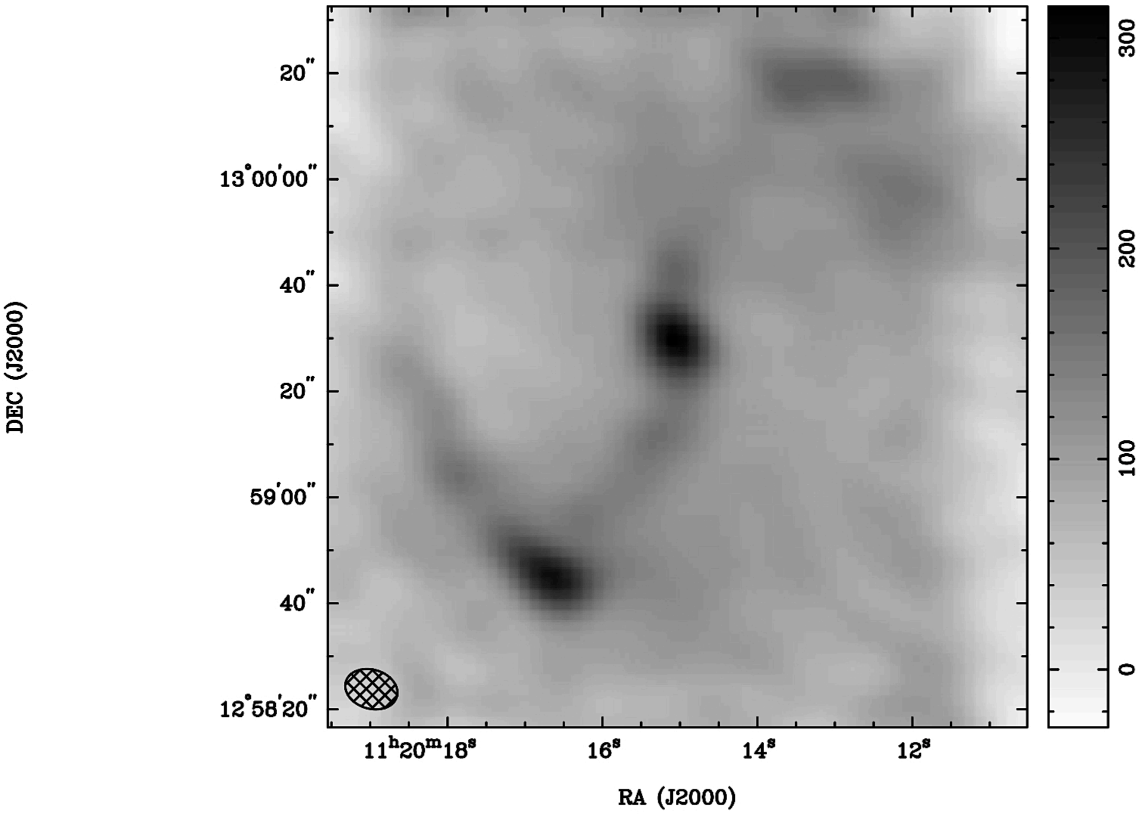

```
RA, DEC, VELO = 11:20:15.100, 12:59:21.60, 2.13945E-03 km/s at pixel (33.00, 33.00, 1.00)
Spatial region : 1,1 to 66,68
Pixel map image: mosmem (NGC3627)  Min/max=-27.52/315  Range = -27.52 to 315 JY/BEAM. (lin)
```

Fig. 18.— Moment 0 map made using MOSMEM. Note how that the distribution of CO along the bar and spiral arms is more defined than it is in Figure 16.

8. Interferometric Observations of Galactic Molecular Clumps

Manuel Merello (University of Texas)

8.1. Motivation

Recent wide-area surveys in millimeter wavelengths have started to explore the dust continuum emission in the Galactic plane. The emission in these wavelengths is considered optically thin, and therefore offers a reliable tracer of column densities. Several groups have made studies of submillimeter emission over small regions (e.g., Enoch et al. 2007, Kauffmann et al. 2008), but the recent development of large bolometer array cameras now provide an opportunity to perform large-scale surveys of massive star-forming regions.

The Bolocam Galactic Plane Survey (BGPS) has mapped the continuum emission at 1.1 mm over nearly 170 square degrees of the northern Galactic plane at a resolution of $33''$. The survey covers contiguously between $l = -10.5$ to $+90.5$ and $|b| \leq 0.5$, extending this range to $|b| \leq 1.5$ in the Cygnus X area ($75.5 \leq l \leq 87.5$) and additional cross cuts to $|b| \leq 1.5$ at $l = 3, 15, 30$ and 31. This gives a covered area of 133 deg^2. In addition, four targeted regions were mapped in the outer galaxy, IC1396, the Perseus Arm near NGC7538, W3/4/5, and GemOB1 that complete the survey. The survey was conducted using the 144-element Bolocam array, installed on the Caltech Submillimeter Observatory (CSO), with a band center of 271.1 GHz and a width of 46 GHz. (See Glenn et al. 2003.) Using Bolocat, a custom algorithm to identify and characterize objects from Bolocam images, the catalog has identified 8358 sources, with a 1-σ noise level of 11-53 mJy/beam (Rosolowsky et al. 2010, Aguirre et al. 2010). For several of these sources, we have additional continuum maps at 350 μm with a resolution of $9''$ obtained with SHARC-II bolometer, also installed in CSO (Merello et al., in preparation).

Massive star-forming regions are usually located at large distances, and that is the reason why high-resolution observations are required to study the physical and chemical properties of these sources. As part of my future research, I am planning a project that involves follow-up observations of selected sources from the BGPS survey.

During CARMA summer school I mapped two sources from this catalog, *BGPS7465* and *BGPS7466*. These sources are located in the GemOB1 molecular cloud, at a distance of 2.10±0.026 kpc (Reid et al. 2009). Dunham et al. 2010 has studied BGPS clumps in the GemOB1 molecular cloud, finding that *BGPS7465* has a virial mass of 244 $\mathrm{M}_\odot$, a column density of 24×10^{21} cm^{-2}, and a radius of 0.5 pc. This region has also been mapped before at high resolution ($4''$) by Saito et al. 2008, revealing that the clump *BGPS7465* has two components. Fig. 19 shows the map at 350 μm with the position of the sources from the BGPS catalog, the image of the region at 1.1 mm and the high-resolution continuum map at 3 mm, which reveals the two components of one of the selected sources.

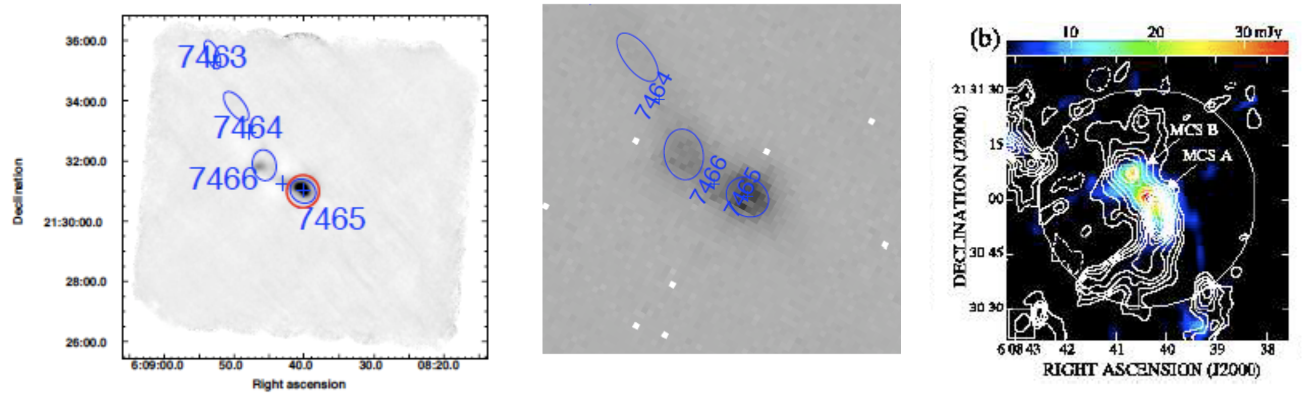

Fig. 19.— *Left:* Image at 350 μm with a resolution of 9″ of the molecular clumps BGPS7465 and BGPS7466 . *Center:* Image of the BGPS survey (1.1 mm) of these region. *Right:* Continuum map at 3 mm with $C^{18}O$ contours for the BGPS7465 molecular clump (Saito et al. 2008).

8.2. Observations and Results

The observations where made with CARMA on July 15, 2010. Using the E-configuration, a 4-point mosaic was obtained during a track of 5 hours and the archived resolution was ∼10″ at 100 GHz. The correlator was configured to obtain four 62 MHz narrow bands and four 500 MHz wide bands. The narrow bands were set to detect CS(2-1) (97.98 GHz), HCN(1-0) (88.63 GHz), $H^{13}CN$(1-0) (86.34 GHz), and HCO^+(1-0) (89.19 GHz). This set of lines will give information related with density and signpost of disk accretion on the sources (e.g., Sandell & Wright 2009). Fig. 20 shows the continuum map at 3 mm obtained for the region, while in Fig. 21 the different maps form the integrated lines are plotted as contours over continuum emission.

From the integrated CS map, the source *BGPS7465* is shown in Fig. 22, along with four particular points on this map. Although a primary beam of 10″ is not enough to resolve the two substructures found by Saito et al. (2008), the peak of the lines on positions B and C has a velocity shift with respect to the other two positions, possibly indicating the presence of the second source. Further analysis is required with these data, but it is clear that CARMA observations are very useful for the characterization of molecular clumps.

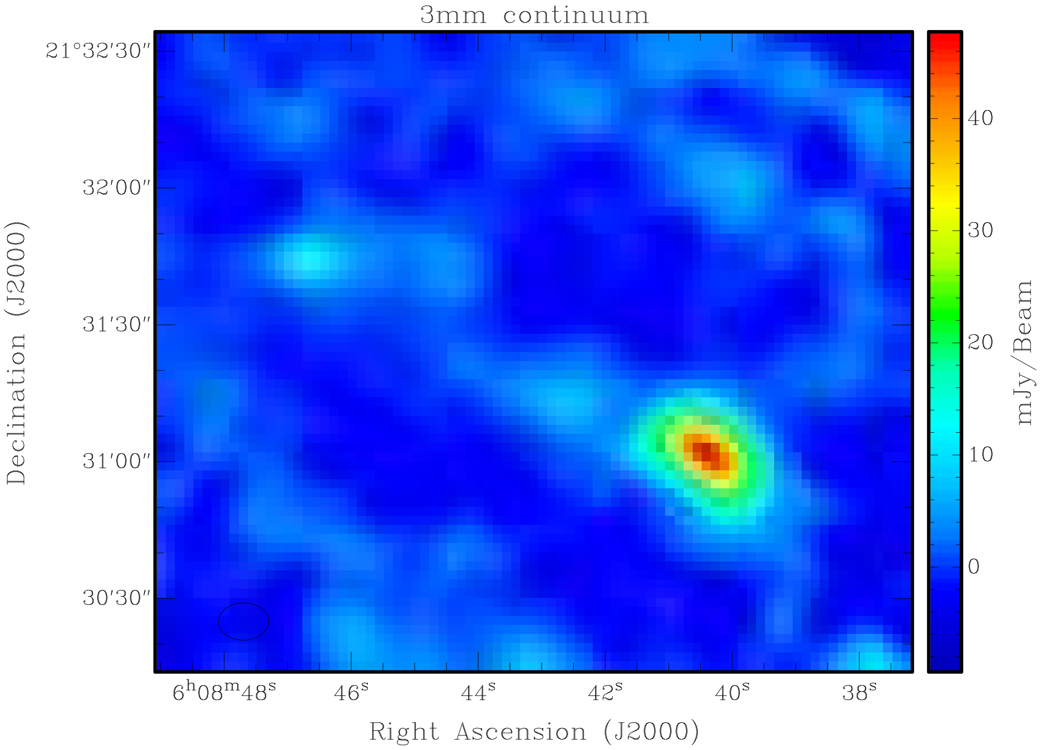

Fig. 20.— Continuum emission map at 3 mm obtained with CARMA. The primary beam size is plotted in the lower-left corner.

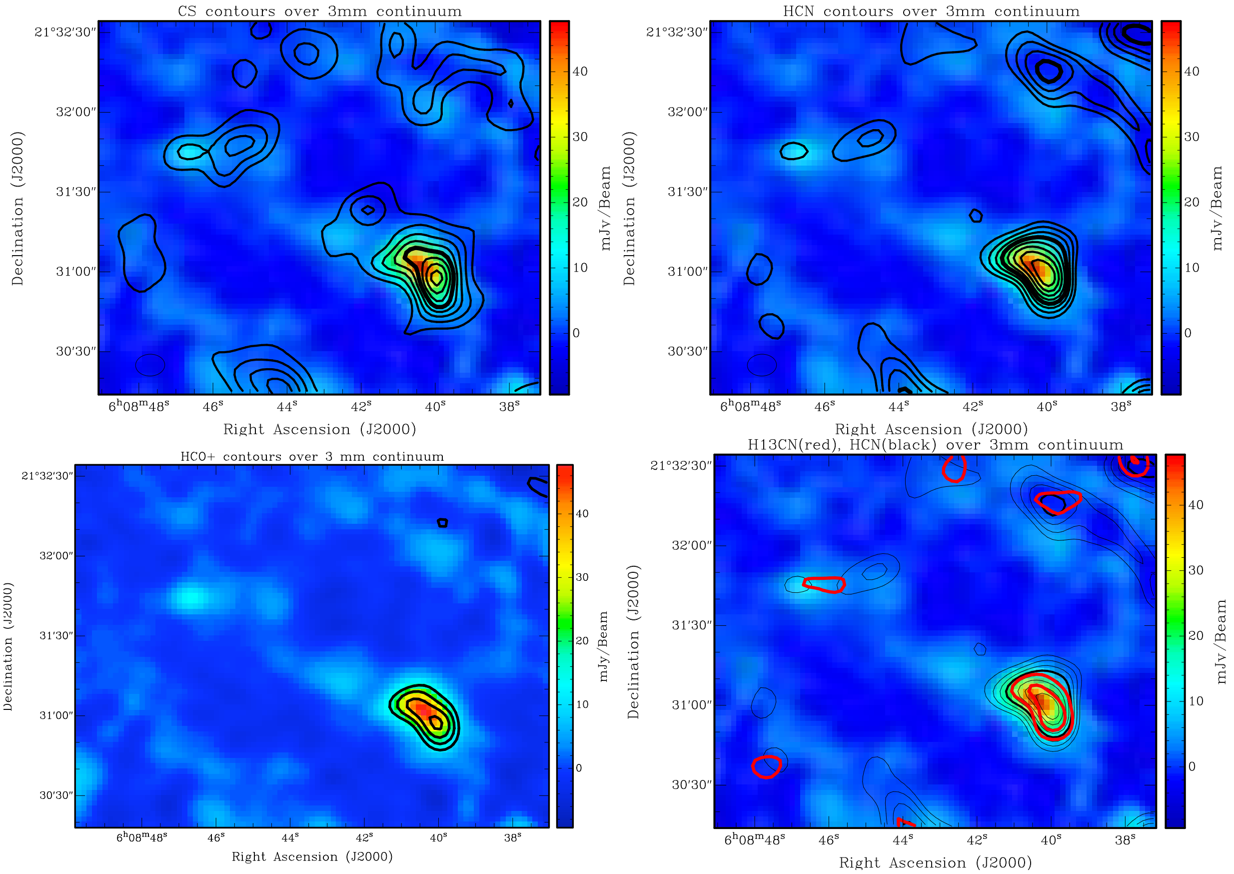

Fig. 21.— Integrated emission line maps plotted as contours over the 3 mm continumm map. *Upper-left:* CS, *Upper-right:* HCN, *Lower-left:* HCO+, *Lower-right:* $H^{13}CN$. The contours in the images are 3σ, $4sigma$, $5sigma$, ... with the exception of $H^{13}CN$, which start on 2σ and are plotted with red contours. In the $H^{13}CN$ map, black contours representing emission of HCN are plotted to compare the distribution of optically thin-optically thick gas.

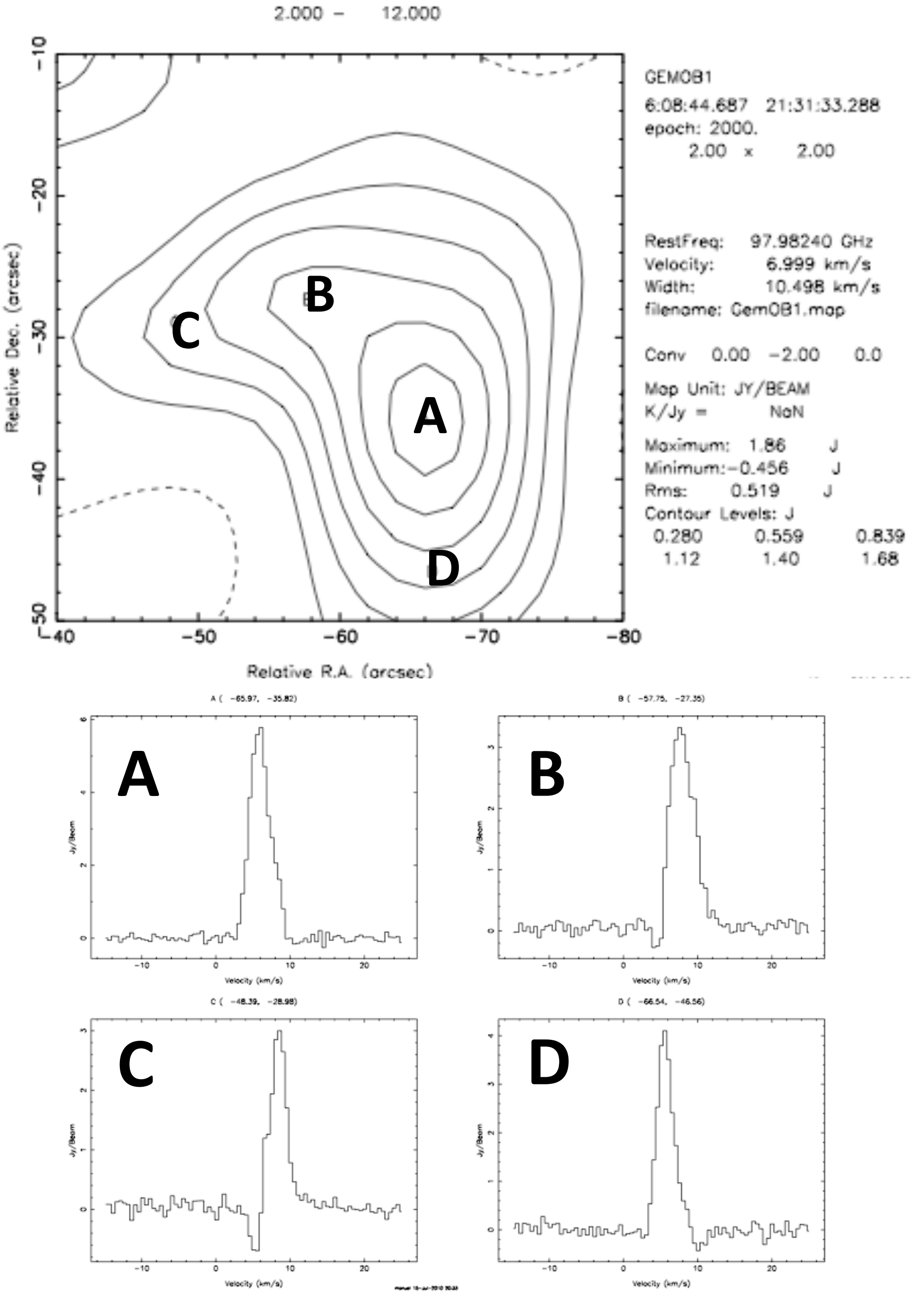

Fig. 22.— *Top:* CS integrated map between 3.6 km s^{-1} and 10 km s^{-1} of the molecular clump. *Lower:* Spectra of four particular points on the CS integrated map. It is probable that the difference in the peak velocity of B and C with respect to A and D is related to a second component on this source.

9. Cygnus A with CARMA at 100GHz

Zubair Abdulla, U. Chicago

9.1. Introduction

Cygnus A is the prototypical two lobed radio galaxy. At the galaxy's center is an active galactic nuclei (AGN), as is with all radio galaxies, from which two symmetric jets extend in opposite directions out to large distances. The high-energy jets terminate in intergalactic medium to produce the observed hotspots and radio lobes. It lies at a redshift of z=.057 and the radio lobes extend $1'$-$2'$ from the galactic nuclei, which corresponds to $\sim$ 60 kpc. As it is understood, particle acceleration occurs at the hotspots due to the jets from the AGN to produce synchrotron radiation. From the hotspots there is outflow which is observed as synchrotron radiation from the extended radio lobes. I investigate the extended structure of Cygnus A with CARMA.

9.2. Observation

Cygnus A lies at RA = 19h59m28.3s DEC = +40d44m02s and extends 2'x2' across the sky. It has been extensively studied in all parts of the spectrum. I used CARMA to map Cygnus A at 100 GHz, with an 8Ghz bandwidth. 5 pointings were observed across the extent of the object then mosaiced to image the full structure of Cygnus A. In the compact E configuration, CARMA is unable to resolve the interesting hotspots, which are about 1 in extent. Our maximum resolution is $\lambda/b \sim$ 5", where lambda is the wavelegnth and b is the longest baseline, 66m. However, the compact configuration gives sensitivity to large angular extent, $\lambda/b \sim$ .5', where b is the shortest baseline 8m, which offers the opportunity to study the extended structure of the radio lobes. The CARMA map of Cygnus A, reduced using MIRIAD, is below in Figure 23. There was overcast for much of the observation night. The structure of the radio galaxy is apparent and can be matched to images in other parts of the spectrum from other radio instruments. The flux at the galactic nucleus is $\sim$ 1Jy/beam, $\sim$ 3Jy/beam - 4Jy/beam near the hotspots, and $\sim$ .1Jy/beam-1Jy/beam in the extended radio lobes at 100 GHz.

9.3. Results and Discussion

This map along with VLA images were used to determine spectral indicies across the lobes. The spectral index is determined by the dependence of the flux of radiation on the frequency, $S \sim \nu^{\alpha}$,, which offers insight into the radiation processes. By taking a logarithm of this relation one can determine the spectral index by $log(S_1/S_2)/log(\nu_1/\nu_2) = \alpha$. By comparing the CARMA 100 GHz map to VLA maps at 5 GHz, 8 GHz, and 15 GHz we can determine spectral indicies across the lobe. The VLA data is higher resolution, so must be deconvolved, downgraded in resolution, then convolved with the CARMA beam in order to compare flux/beam. Maps of the spectral indicies by comparing 100 GHz to 15 GHz and 5 GHz are below in Figures 24 and 25, respectively. The spectral index is consistent with synchrotron radiation, $\alpha \sim -.7$ near the hotspot, but is not consistent between maps across the entire spectrum, as will be discussed. It is interesting to determine the spectrum of the radio lobes. Because synchrotron radiation depletes high-energy electrons first, the spectrum at high-frequencies will steepen, changing the spectral index, and by measuring the spectrum one can attempt to determine the synchrotron age of the radio lobes. The spectrum steepens as one moves further from the hotspot within the radio lobe to show there is evolution of the synchrotron radiation. However, this steepening is also dependent on the source of energy input into the radio lobes. We will not discuss in detail different models for energy input. They are discussed in Carilli et al. (1991). This process will produce a break frequency, below which the spectrum will dominated by newly added particles, and above which the spectrum will be steeper due to synchrotron emission. The shape above and below the break frequency is determined by the mechanism for energy input. The break frequency beyond which the spectrum steepens and the strength of the magnetic field determine the synchrotron age of the object, equation. A naive estimate ($B = 50\mu G$) of this quantity suggests the the hotspots are $\sim$ 1 Myrs and the lobes are $\sim$ 2-3 Myrs; it is atleast apparent the synchrotron age of the lobes are higher than the hotspots. In the hotspots, the spectrum is flatter than in the lobes, which suggests high-energy particles are deposited in hotspots and lose energy in the extended parts of the radio lobes, consistent with current understanding of the lobes dynamics. Jets from the AGN terminate with shocks to deposit energy in the hotspot which accelerate particles to produce synchrotron emission. The material then expands from the hotspots to produce the radio lobes. Because the hotspot spectrum is flatter than the extended radio lobes there is additional energy being deposited into the hotspots by the jets. Comparing with Carilli et al. (1991) and inspection of the spectrum, 100 GHz CARMA data suggests a continuous injection model from the jets. Results of analysis show consistency with previous work, Carilli et al. (1991), Wright et al. (1996), Wright et al. (2004). In addition, the observation is more extended in angular scale than previous work and remains consistent. Understanding the extended structure of the radio lobes should continue to offer insight into the astrophysics of the outflow from the hotspots and evolution of synchrotron emission.

9.4. Figures

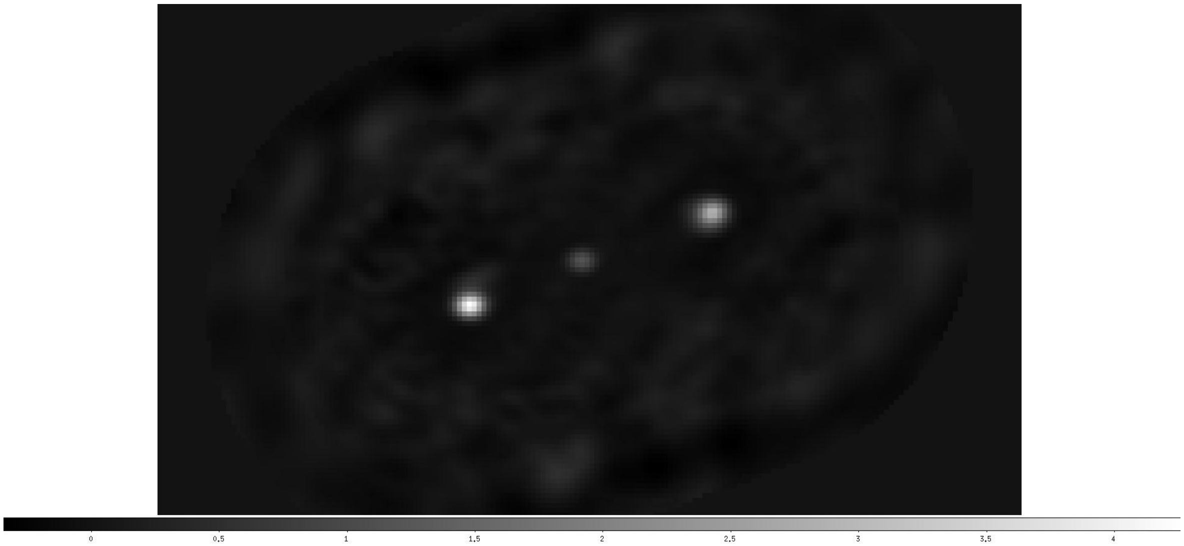

Fig. 23.— CARMA image of Cygnus A at 100GHz. Structure in the two symmetric lobes are apparent. The hots spots remain unresolved. 5 pointings across the strucure were mosaiced to produce the image. The map is approxiamtely 2'x2', units are in Jy/beam

Fig. 24.— Spectral index, α, across the radio lobes by comparing CARMA map at 100 GHz and VLA map at 15GHz convolved to a lower resolution. α becomes more negative (spectrum steepens) further from the hotspots, suggesting evolution of the radiation.

Fig. 25.— Spectral index, α, across the radio lobes by comparing CARMA map at 100 GHz and VLA map at 5GHz convolved to a lower resolution. α is steeper than in above map of spectral indicies. This offers insight into the shape of the spectrum and thus the astrophysical mechanism providing the energy input

E-mail addresses

`Swarnima Manohar (CIT), smanohar@astro.caltech.edu`
`Thiago Goncalves (CIT), tsg@astro.caltech.edu`
`Mislav Balokovic (University of Split/CIT),  mislavb@pmfst.hr`
`David Fisher (UMD),twitch@spitzer.as.utexas.edu`
`Rodrigo Herrera Camus (UMD), riherrera@gmail.com`
`Katie Jameson (UMD), ktjameson@gmail.com`
`Ben Westbrook (UCB), jamin.westbrook@gmail.com`
`Zubair Abdulla (Chicago), zabdulla@oddjob.uchicago.edu`
`Felippe Navarrete (Max Planck), fpnavarr@mpifr-bonn.mpg.de`
`Rie Miura (U Tokyo), rie.miura@nao.ac.jp`
`Adele Plunkett (Yale), adele.plunkett@yale.edu`
`Jason Speights (NM Inst of Mining and Tech), jspeight@nmt.edu`
`Tim Weinzirl (U of Texas), timw@astro.as.utexas.edu`
`Manuel Merello (U of Texas), manuel@astro.as.utexas.edu`
`Thomas Fok Kai Tung (U of Hong Kong), h0401027@hku.hk`
`Marc Royster (Northwestern), mjroyster@u.northwestern.edu`
`Zubair Abdulla (Chicago), zabdulla@oddjob.uchicago.edu`

REFERENCES

Aguirre, J., et al. 2009, ApJ, submitted

Bally et al. 1987, ApJS, 65, 13 MNRAS, 252, 210

Binney et al. 1991,

Carilli, C. L. and Perley, R. A. and Dreher, J. W. and Leahy, J. P. 1991, ApJ, 383, 554

Condon, J. J. 1992, ARA&A, 30, 575

Condon, J. J., Cotton, W. D., Greisen, E. W., Yin, Q. F., Perley, R. A., Taylor, G. B., & Broderick, J. J. 1998, AJ, 115, 1693

Dunham, M. K., et al. 2010, ApJ, 717, 1157

Enoch, M. L., Glenn, J., Evans, N. J., II, Sargent, A. I., Young, K. E., & Huard, T. L. 2007, ApJ, 666, 982

Glenn, J., et al. 2003, Proc. SPIE, 4855, 30

Hodges–Kluck et al. 2009, ApJ, 696, 1374

Kauffmann, J., Bertoldi, F., Bourke, T. L., Evans, N. J., II, & Lee, C. W. 2008, A&A, 487, 993

Knox, L., Holder, G. P., & Church, S. E. 2004, ApJ, 612, 96

Lee, C.W. 1996, ApJS, 105, 129

Lin, Y., & Mohr, J. J. 2007, ApJS, 170, 71

Lin, Y., Partridge, B., Pober, J. C., Bouchefry, K. E., Burke, S., Klein, J. N., Coish, J. W., & Huffenberger, K. M. 2009, ApJ, 694, 992

Nakashima, J. & Deguchi, S. 2005, ApJ, 633, 282

Reid, M. J., et al. 2009, ApJ, 700, 137

Rosolowsky, E., et al. 2010, ApJS, 188, 123

Sadler, E. M., Ricci, R., Ekers, R. D., Sault, R. J., Jackson, C. A., & de Zotti, G. 2008, MNRAS, 385, 1656

Sandell, G., & Knee, L. B. G. 2001, ApJL, 546, L49

Sandell, G., & Wright, M. 2010, ApJ, 715, 919

Sunyaev, R. A., & Zeldovich, Y. B. 1970, Ap&SS, 7, 3

Wright, M. C. H. and Chernin, L. M. and Forster, J. R. 1996, ApJ, 483, 783

Wright, M. C. H. and Birkinshaw, M. 2004, ApJ, 614, 115